

**Electronic states and cyclotron resonance in  $n$ -type InMnAs**

G. D. Sanders, Y. Sun, F. V. Kyrychenko, and C. J. Stanton

*Department of Physics, University of Florida, Box 118440, Gainesville, Florida 32611-8440, USA*

G. A. Khodaparast, M. A. Zudov,\* and J. Kono

*Department of Electrical and Computer Engineering, Rice University, Houston, Texas 77005, USA*Y. H. Matsuda<sup>†</sup> and N. Miura*Institute for Solid State Physics, University of Tokyo, Kashiwanoha, Kashiwa, Chiba 277-8581, Japan*

H. Munekata

*Imaging Science and Engineering Laboratory, Tokyo Institute of Technology, Yokohama, Kanagawa 226-8503, Japan*

(Received 18 April 2003; published 23 October 2003)

We present a theory for electronic and magneto-optical properties of  $n$ -type  $\text{In}_{1-x}\text{Mn}_x\text{As}$  magnetic alloy semiconductors in a high magnetic field  $B\parallel\hat{z}$ . We use an eight-band Pidgeon-Brown model generalized to include the wave vector ( $k_z$ ) dependence of the electronic states as well as  $s$ - $d$  and  $p$ - $d$  exchange interactions with localized Mn  $d$  electrons. Calculated conduction-band Landau levels exhibit effective masses and  $g$  factors that are strongly dependent on temperature, magnetic field, Mn concentration ( $x$ ), and  $k_z$ . Cyclotron resonance (CR) spectra are computed using Fermi's golden rule and compared with ultrahigh-magnetic-field ( $>50$  T) CR experiments, which show that the electron CR peak position is sensitive to  $x$ . Detailed comparison between theory and experiment allowed us to extract the  $s$ - $d$  and  $p$ - $d$  exchange parameters  $\alpha$  and  $\beta$ . We find that not only  $\alpha$  but also  $\beta$  affects the electron mass because of the strong interband coupling in this narrow-gap semiconductor. In addition, we derive analytical expressions for effective masses and  $g$  factors within the eight-band model. Results indicate that  $(\alpha-\beta)$  is the crucial parameter that determines the exchange interaction correction to the cyclotron masses. These findings should be useful for designing novel devices based on ferromagnetic semiconductors.

DOI: 10.1103/PhysRevB.68.165205

PACS number(s): 75.50.Pp, 78.20.Ls, 78.40.Fy

**I. INTRODUCTION**

Recently, there has been much interest in III-V magnetic semiconductors such as InMnAs (Ref. 1) and GaMnAs (Ref. 2). The ferromagnetic exchange coupling between Mn ions in these semiconductors is believed to be mediated by free holes that are provided by Mn acceptors. They become ferromagnetic at low temperatures and high enough Mn concentrations. Recent innovative experiments have demonstrated the feasibility of controlling ferromagnetism in these systems by tuning the carrier density optically<sup>3</sup> and electrically.<sup>4</sup> Understanding their electronic, transport, and optical properties is crucial for designing novel ferromagnetic semiconductor devices with high Curie temperatures. However, basic band parameters such as effective masses and  $g$  factors have not been accurately determined. InMnAs alloys and their heterostructures with AlGaSb, the first grown III-V magnetic semiconductor,<sup>1,5,6</sup> serve as a prototype for implementing electron and hole spin degrees of freedom in semiconductor spintronic devices.

The localized Mn spins strongly influence the delocalized conduction and valence-band states through the  $s$ - $d$  and  $p$ - $d$  exchange interactions. These interactions are usually parametrized as  $\alpha$  and  $\beta$ , respectively.<sup>7</sup> Determining these parameters is important for understanding the nature of Mn electron states and their mixing with delocalized carrier states. In narrow-gap semiconductors like InMnAs, due to strong interband mixing,  $\alpha$  and  $\beta$  can influence *both* the conduction and valence bands. This is in contrast to wide-gap semicon-

ductors where  $\alpha$  influences primarily the conduction band and  $\beta$  the valence band. In addition, in narrow-gap semiconductors, due to the strong interband mixing, the coupling to the Mn spins does not affect all Landau levels by the same amount. As a result, the electron cyclotron resonance (CR) peak can shift as a function of the Mn concentration  $x$ . This can be a sensitive method for estimating these exchange parameters. For example, a recent CR study of  $\text{Cd}_{1-x}\text{Mn}_x\text{Te}$  (Ref. 8) showed that the electron mass is strongly affected by  $sp$ - $d$  hybridization.

In a recent Rapid Communication,<sup>9</sup> we reported the first observation of electron CR in  $n$ -type  $\text{In}_{1-x}\text{Mn}_x\text{As}$  films and described the dependence of cyclotron mass on  $x$ , ranging from 0 to 12%. We observe that the electron CR peak shifts to lower field with increasing  $x$ . Midinfrared interband absorption spectroscopy revealed no significant  $x$  dependence of the band gap. A detailed comparison of experimental results with calculations based on a modified Pidgeon-Brown model allowed us to estimate  $\alpha$  and  $\beta$  to be 0.5 eV and  $-1.0$  eV, respectively.

In this paper, we describe details of the theoretical model and comparison with the experiments. We use an eight-band Pidgeon-Brown model, which is generalized to include the wave vector ( $k_z$ ) dependence of the electronic states as well as  $s$ - $d$  and  $p$ - $d$  exchange interactions with localized Mn  $d$  electrons. Calculated conduction-band Landau levels exhibit effective masses and  $g$  factors that are strongly dependent on temperature, magnetic field, Mn doping  $x$ , and  $k_z$ . At low

TABLE I. Densities, mobilities, and cyclotron masses for the four samples studied. The densities and mobilities are in units of  $\text{cm}^{-3}$  and  $\text{cm}^2/\text{Vs}$ , respectively. The masses were obtained at a photon energy of 117 meV (or  $\lambda = 10.6 \mu\text{m}$ ).

Mn content $x$	0	0.025	0.050	0.120
Density (4.2 K)	$\sim 1.0 \times 10^{17}$	$1.0 \times 10^{16}$	$0.9 \times 10^{16}$	$1.0 \times 10^{16}$
Density (290 K)	$\sim 1.0 \times 10^{17}$	$2.1 \times 10^{17}$	$1.8 \times 10^{17}$	$7.0 \times 10^{16}$
Mobility (4.2 K)	$\sim 4000$	1300	1200	450
Mobility (290 K)	$\sim 4000$	400	375	450
$m/m_0$ (30 K)	0.0342	0.0303	0.0274	0.0263
$m/m_0$ (290 K)	0.0341	0.0334	0.0325	0.0272

temperatures and high  $x$ , the sign of the  $g$  factor is positive and its magnitude exceeds 100. CR spectra are computed using Fermi's golden rule. We also derive analytical expressions for effective masses and  $g$  factors within the eight-band model, which indicates that  $(\alpha - \beta)$  is the crucial parameter that determines the exchange interaction correction to the cyclotron masses. These findings should be useful for designing novel devices based on ferromagnetic semiconductors.

## II. EXPERIMENT

We studied four  $\sim 2\text{-}\mu\text{m}$ -thick  $\text{In}_{1-x}\text{Mn}_x\text{As}$  films with manganese concentrations  $x=0, 0.025, 0.050,$  and  $0.120$  by ultrahigh-field magnetoabsorption spectroscopy. The films were grown by low temperature molecular beam epitaxy on semi-insulating GaAs substrates at  $200^\circ\text{C}$ . All the samples were  $n$  type and did not show ferromagnetism down to  $1.5\text{ K}$ . The electron densities and mobilities deduced from Hall measurements are listed in Table I, together with the electron cyclotron masses obtained at a photon energy of 117 meV (or a wavelength of  $10.6 \mu\text{m}$ ).

The single-turn coil technique<sup>10</sup> was used to generate ultrahigh magnetic fields with a pulse duration of  $\sim 7 \mu\text{s}$ . The sample and pickup coil were placed in a liquid helium flow cryostat. The single-turn coil breaks in the outward direction, leaving the sample, the pickup coil, and the cryostat intact, which allows us to repeat such destructive pulsed measurements on the same sample. We used the  $10.6\text{-}\mu\text{m}$  line from a  $\text{CO}_2$  laser and produced circular polarization using a CdS quarter-wave plate. The transmitted radiation was detected by a fast HgCdTe photovoltaic detector. Signals from the detector and pickup coil were transmitted via optical fiber to a multichannel digitizer located in a shielded measurement room.

Typical measured CR spectra at 30 K and 290 K are shown in Figs. 1(a) and 1(b), respectively. Note that to compare the transmission with absorption calculations, the transmission increases in the negative  $y$  direction. Each figure shows spectra for all four samples labeled by the corresponding Mn compositions from 0 to 12%. All the samples show pronounced absorption peaks (or transmission dips) and the resonance field *decreases* with increasing  $x$ . Increasing  $x$  from 0 to 12% results in a  $\sim 25\%$  decrease in cyclotron mass (see Table I). It is important to note that at resonance, the densities and fields are such that only the lowest Landau level for each spin type is occupied (see Fig. 3). Thus, all the

electrons were in the lowest Landau level for a given spin even at room temperature, precluding any density-dependent mass due to nonparabolicity (expected at zero or low magnetic fields) as the cause of the observed trend.

At high temperatures [e.g., Fig. 1(b)] the  $x=0$  sample clearly shows nonparabolicity-induced CR spin splitting with the weaker (stronger) peak originating from the lowest spin-down (spin-up) Landau level, while the other three samples do not show such splitting. The reason for the absence of splitting in the Mn-doped samples is a combination of (1) their low mobilities (which lead to substantial broadening) and (2) the large effective  $g$  factors due to the Mn ions; especially in samples with large  $x$  only the spin-down level is substantially thermally populated (cf. Fig. 3).

We also performed midinfrared interband absorption measurements at various temperatures using Fourier-transform infrared spectroscopy to determine how the band gap changes with Mn doping  $x$ . In Fig. 2 we show transmission spectra for the four samples at two temperatures (30 K and 300 K). While a shift can be seen in the band gap in the  $x=0$  samples, we attribute this to a pronounced Burstein-Moss shift resulting from the large electron density of the  $x=0$  sample. (As one increases the Mn doping, the electron density diminishes rapidly since the Mn ions act as accep-

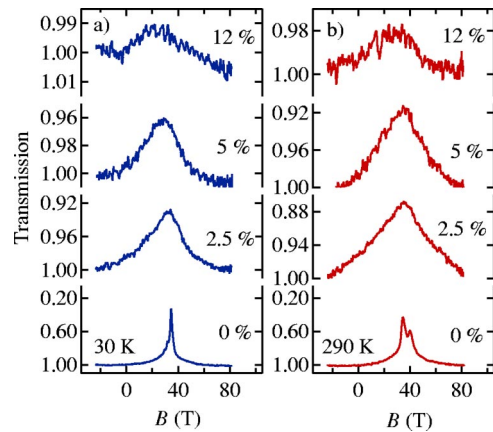


FIG. 1. Experimental CR spectra for different Mn concentrations  $x$  taken at 290 (a) and 30 K (b). The wavelength of the laser was fixed at  $10.6 \mu\text{m}$  with electron-active circular polarization while the magnetic field  $B$  was swept. The resonance position shifts to lower  $B$  with increasing  $x$ . The  $x$  values are 0%, 2.5%, 5%, and 12%.

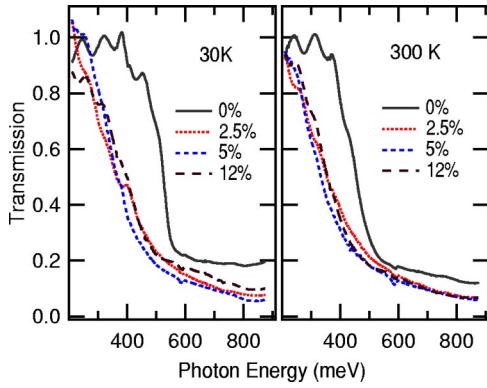


FIG. 2. Midinfrared transmission spectra for the four samples studied, taken at 30 K and 300 K. The shift in band gap for the  $x=0$  sample can be attributed to a pronounced Burstein-Moss shift resulting from the large electron density in the  $x=0$  sample.

tors). The Fermi energy for an electron density of  $1 \times 10^{18} \text{ cm}^{-3}$  with a mass of  $0.023m_0$  is 135 meV (without including the nonparabolicity). This roughly accounts for the observed large shift in the absorption edge. Thus, our experimental data indicates that band gap does not depend strongly on the Manganese concentration  $x$ .

### III. THEORY

In this section we describe our effective mass theory of the electronic and optical properties of  $n$ -type  $\text{In}_{1-x}\text{Mn}_x\text{As}$  alloys. Our method is based on the Pidgeon-Brown<sup>11</sup> effective mass model of narrow-gap semiconductors in a magnetic field which includes the conduction electrons, heavy holes, light holes, and split-off holes for a total of eight bands when spin is taken into account. In the original Pidgeon-Brown paper, only the zone center  $k_z=0$  states were considered and magnetic impurity effects were not included.

The eight-band Pidgeon-Brown model can be generalized to include the wave vector ( $k_z$ ) dependence of the electronic states as well as the  $s$ - $d$  and  $p$ - $d$  exchange interactions with localized Mn  $d$  electrons.<sup>12</sup>

The magneto-optical and cyclotron absorption can then be computed using electronic states obtained from the generalized Pidgeon-Brown model and Fermi's golden rule. We will describe this in detail below.

#### A. Effective mass Hamiltonian

Following Pigeon and Brown<sup>11</sup> we find it convenient to separate the eight Bloch basis states into an upper and lower set which decouple at the zone center, i.e.,  $k_z=0$ . The Bloch basis states for the upper set are

$$|1\rangle = \left| \frac{1}{2}, +\frac{1}{2} \right\rangle = |S\uparrow\rangle, \quad (1a)$$

$$|2\rangle = \left| \frac{3}{2}, +\frac{3}{2} \right\rangle = \frac{1}{\sqrt{2}} |(X+iY)\uparrow\rangle, \quad (1b)$$

$$|3\rangle = \left| \frac{3}{2}, -\frac{1}{2} \right\rangle = \frac{1}{\sqrt{6}} |(X-iY)\uparrow + 2Z\downarrow\rangle, \quad (1c)$$

$$|4\rangle = \left| \frac{1}{2}, -\frac{1}{2} \right\rangle = \frac{i}{\sqrt{3}} |-(X-iY)\uparrow + Z\downarrow\rangle, \quad (1d)$$

which correspond to electron spin up, heavy hole spin up, light hole spin down, and split-off hole spin down. Likewise, the Bloch basis states for the lower set are

$$|5\rangle = \left| \frac{1}{2}, -\frac{1}{2} \right\rangle = |S\downarrow\rangle, \quad (2a)$$

$$|6\rangle = \left| \frac{3}{2}, -\frac{3}{2} \right\rangle = \frac{i}{\sqrt{2}} |(X-iY)\downarrow\rangle, \quad (2b)$$

$$|7\rangle = \left| \frac{3}{2}, +\frac{1}{2} \right\rangle = \frac{i}{\sqrt{6}} |(X+iY)\downarrow - 2Z\uparrow\rangle, \quad (2c)$$

$$|8\rangle = \left| \frac{1}{2}, +\frac{1}{2} \right\rangle = \frac{1}{\sqrt{3}} |(X+iY)\downarrow + Z\uparrow\rangle, \quad (2d)$$

corresponding to electron spin down, heavy hole spin down, light hole spin up, and split-off hole spin up.

The effective mass Hamiltonian in bulk zinc-blende materials is given explicitly in Ref. 13. In the presence of a uniform magnetic field  $B$  oriented along the  $z$  axis, the wave vector  $\vec{k}$  in the effective mass Hamiltonian is replaced by the operator

$$\vec{k} = \frac{1}{\hbar} \left( \vec{p} + \frac{e}{c} \vec{A} \right), \quad (3)$$

where  $\vec{p} = -i\hbar \vec{\nabla}$  is the momentum operator and  $\vec{A}$  is the vector potential. For the vector potential, we choose the Landau gauge

$$\vec{A} = -By\hat{x}, \quad (4)$$

from which we obtain  $\vec{B} = \vec{\nabla} \times \vec{A} = B\hat{z}$ .

We introduce the appropriate creation and destruction operators

$$a^\dagger = \frac{\lambda}{\sqrt{2}} (k_x + ik_y), \quad (5a)$$

and

$$a = \frac{\lambda}{\sqrt{2}} (k_x - ik_y). \quad (5b)$$

The magnetic length  $\lambda$  is

$$\lambda = \sqrt{\frac{\hbar c}{eB}} = \sqrt{\frac{\hbar^2}{2m_0 \mu_B B}}, \quad (6)$$

where  $\mu_B = 5.789 \times 10^{-5} \text{ eV/T}$  is the Bohr magneton and  $m_0$  is the free electron mass. Using Eqs. (5a) and (5b) to elimi-

nate the operators  $k_x$  and  $k_y$  in the effective mass Hamiltonian, we arrive at the Landau Hamiltonian

$$H_L = \begin{bmatrix} L_a & L_c \\ L_c^\dagger & L_b \end{bmatrix}, \quad (7)$$

with the submatrices  $L_a$ ,  $L_b$ , and  $L_c$  given by

$$L_a = \begin{bmatrix} E_g + A & i\frac{V}{\lambda}a^\dagger & i\sqrt{\frac{1}{3}}\frac{V}{\lambda}a & \sqrt{\frac{2}{3}}\frac{V}{\lambda}a \\ -i\frac{V}{\lambda}a & -P - Q & -M & i\sqrt{2}M \\ -i\sqrt{\frac{1}{3}}\frac{V}{\lambda}a^\dagger & -M^\dagger & -P + Q & i\sqrt{2}Q \\ \sqrt{\frac{2}{3}}\frac{V}{\lambda}a^\dagger & -i\sqrt{2}M^\dagger & -i\sqrt{2}Q & -P - \Delta \end{bmatrix}, \quad (8)$$

$$L_b = \begin{bmatrix} E_g + A & -\frac{V}{\lambda}a & -\sqrt{\frac{1}{3}}\frac{V}{\lambda}a^\dagger & i\sqrt{\frac{2}{3}}\frac{V}{\lambda}a^\dagger \\ -\frac{V}{\lambda}a^\dagger & -P - Q & -M^\dagger & i\sqrt{2}M^\dagger \\ -\sqrt{\frac{1}{3}}\frac{V}{\lambda}a & -M & -P + Q & i\sqrt{2}Q \\ -i\sqrt{\frac{2}{3}}\frac{V}{\lambda}a & -i\sqrt{2}M & -i\sqrt{2}Q & -P - \Delta \end{bmatrix}, \quad (9)$$

$$L_c = \begin{bmatrix} 0 & 0 & \sqrt{\frac{2}{3}}Vk_z & i\sqrt{\frac{1}{3}}Vk_z \\ 0 & 0 & -L & -i\sqrt{\frac{1}{2}}L \\ -i\sqrt{\frac{2}{3}}Vk_z & L & 0 & i\sqrt{\frac{3}{2}}L^\dagger \\ -\sqrt{\frac{1}{3}}Vk_z & -i\sqrt{\frac{1}{2}}L & i\sqrt{\frac{3}{2}}L^\dagger & 0 \end{bmatrix}. \quad (10)$$

In Eq. (7),  $E_g$  is the bulk band gap, and  $\Delta$  is the spin-orbit splitting. The Kane momentum matrix element  $V = (-i/\hbar) \times \langle S|p_x|X \rangle$  is related to the optical matrix parameter  $E_p$  by<sup>14</sup>

$$V = \sqrt{\frac{\hbar^2}{m_0}} \frac{E_p}{2}. \quad (11)$$

The operators  $A$ ,  $P$ ,  $Q$ ,  $L$ , and  $M$  are

$$A = \frac{\hbar^2}{m_0} \frac{\gamma_4}{2} \left( \frac{2N+1}{\lambda^2} + k_z^2 \right), \quad (12a)$$

$$P = \frac{\hbar^2}{m_0} \frac{\gamma_1}{2} \left( \frac{2N+1}{\lambda^2} + k_z^2 \right), \quad (12b)$$

$$Q = \frac{\hbar^2}{m_0} \frac{\gamma_2}{2} \left( \frac{2N+1}{\lambda^2} - 2k_z^2 \right), \quad (12c)$$

$$L = \frac{\hbar^2}{m_0} \gamma_3 \left( \frac{-i\sqrt{6}k_z a}{\lambda} \right), \quad (12d)$$

and

$$M = \frac{\hbar^2}{m_0} \left( \frac{\gamma_2 + \gamma_3}{2} \right) \left( \frac{\sqrt{3}}{\lambda^2} a^2 \right). \quad (12e)$$

In Eq. (12e), we have neglected a second term in  $M$  proportional to  $(\gamma_2 - \gamma_3)(a^\dagger)^2$ . We do this for two reasons: (1)  $(\gamma_2 - \gamma_3)$  is small and (2) this term will couple different Landau manifolds, making it more difficult to diagonalize the Hamiltonian. The effect of this term can be accounted for later by perturbation theory.

In Eq. (12), the number operator  $N = a^\dagger a$ . The parameters  $\gamma_1$ ,  $\gamma_2$ , and  $\gamma_3$  used here are not the usual Luttinger parameters since this is an eight-band model, but instead are related to the usual Luttinger parameters  $\gamma_1^L$ ,  $\gamma_2^L$ , and  $\gamma_3^L$  through the relations<sup>15</sup>

$$\gamma_1 = \gamma_1^L - \frac{E_p}{3E_g}, \quad (13)$$

$$\gamma_2 = \gamma_2^L - \frac{E_p}{6E_g}, \quad (14)$$

and

$$\gamma_3 = \gamma_3^L - \frac{E_p}{6E_g}. \quad (15)$$

This takes into account the additional coupling of the valence bands to the conduction band not present in the six-band Luttinger model.

The parameter  $\gamma_4$  is related to the conduction-band electron effective mass  $m_e^*$  through the relation<sup>13</sup>

$$\gamma_4 = \frac{1}{m_e^*} - \frac{E_p}{3} \left( \frac{2}{E_g} + \frac{1}{E_g + \Delta} \right). \quad (16)$$

Note that  $\gamma_4$  can be related to the Kane parameter  $F$ ,

$$F = \frac{1}{m_0} \sum_r \frac{|\langle S|p_x|u_r \rangle|^2}{(E_c - E_r)}, \quad (17)$$

by  $\gamma_4 = 1 + 2F$ . In Eq. (17),  $\langle S|p_x|u_r \rangle$  is the momentum matrix element between the  $s$ -like conduction bands with energies near  $E_c$  and remote bands  $r$  with characteristic energies  $E_r$ . The Kane parameter  $F$  takes into account the higher, remote-band contributions to the conduction band through second-order perturbation theory.<sup>14</sup>

The Zeeman Hamiltonian is

$$H_Z = \frac{\hbar^2}{m_0} \frac{1}{\lambda^2} \begin{bmatrix} Z_a & 0 \\ 0 & -Z_a \end{bmatrix}, \quad (18)$$

where the  $4 \times 4$  submatrix  $Z_a$  is given by

$$Z_a = \begin{bmatrix} \frac{1}{2} & 0 & 0 & 0 \\ 0 & -\frac{3}{2}\kappa & 0 & 0 \\ 0 & 0 & \frac{1}{2}\kappa & -i\sqrt{\frac{1}{2}}(\kappa+1) \\ 0 & 0 & i\sqrt{\frac{1}{2}}(\kappa+1) & \kappa + \frac{1}{2} \end{bmatrix}. \quad (19)$$

The value of  $\kappa$  used in Eq. (19) is related to  $\kappa^L$  as defined by Luttinger through the relation<sup>15</sup>

$$\kappa = \kappa^L - \frac{E_p}{6E_g}. \quad (20)$$

For the Luttinger parameter  $\kappa^L$ , we use the approximation<sup>11,16,17</sup>

$$\kappa^L = \gamma_3^L + \frac{2}{3}\gamma_2^L - \frac{1}{3}\gamma_1^L - \frac{2}{3}. \quad (21)$$

The exchange interaction between the  $\text{Mn}^{++}$   $d$  electrons and the conduction  $s$  and valence  $p$  electrons is treated in the virtual crystal and molecular field approximation. The resulting Mn exchange Hamiltonian is<sup>12</sup>

$$H_{Mn} = xN_0 \langle S_z \rangle \begin{bmatrix} D_a & 0 \\ 0 & -D_a \end{bmatrix}, \quad (22)$$

where  $x$  is the Mn concentration,  $N_0$  is the number of cation sites in the sample, and  $\langle S_z \rangle$  is the average spin on a Mn site. The  $4 \times 4$  submatrix  $D_a$  is

$$D_a = \begin{bmatrix} \frac{1}{2}\alpha & 0 & 0 & 0 \\ 0 & \frac{1}{2}\beta & 0 & 0 \\ 0 & 0 & -\frac{1}{6}\beta & -i\frac{\sqrt{2}}{3}\beta \\ 0 & 0 & i\frac{\sqrt{2}}{3}\beta & \frac{1}{2}\beta \end{bmatrix}, \quad (23)$$

where  $\alpha$  and  $\beta$  are the exchange integrals.

In the paramagnetic phase, the average spin on a Mn site is given in the limit of noninteracting spins by

$$\langle S_z \rangle = -SB_S \left( gS \frac{\mu_B B}{kT} \right), \quad (24)$$

where  $g=2$  and  $S=\frac{5}{2}$  for the  $3d^5$  electrons of the  $\text{Mn}^{++}$  ion.<sup>7</sup> The Brillouin function  $B_S(x)$  is defined as

$$B_S(x) = \frac{2S+1}{2S} \coth \left( \frac{2S+1}{2S} x \right) - \frac{1}{2S} \coth \left( \frac{x}{2S} \right). \quad (25)$$

The antiparallel orientation of  $B$  and  $\langle S_z \rangle$  is due to the difference in sign of the magnetic moment and the electron spin. Since  $B$  is directed along the  $z$  axis, the average Mn spin saturates at  $\langle S_z \rangle = -\frac{5}{2}$ .

The total effective mass Hamiltonian for  $\text{In}_{1-x}\text{Mn}_x\text{As}$  in a magnetic field directed along the  $z$  axis is just the sum of the Landau, Zeeman, and  $sp$ - $d$  exchange contributions, i.e.,

$$H = H_L + H_Z + H_{Mn}. \quad (26)$$

We note that at  $k_z=0$ , the effective mass Hamiltonian is block diagonal with respect to the upper and lower Bloch basis sets.

It is assumed in our calculations that the compensation arises from As antisites and hence the effective Mn fraction  $x$  in Eq. (22) is taken to be equal to the actual Mn fraction in the sample. We note that this is supported by experimental evidence showing that InAs grown at low temperature (200 °C) is a homogeneous alloy and that the magnetization varies linearly with Mn content  $x$ .<sup>1,18–20</sup>

## B. Energies and wave functions

With the choice of gauge given in Eq. (4), translational symmetry in the  $x$  direction is broken while translational symmetry along the  $y$  and  $z$  directions is maintained. Thus,  $k_y$  and  $k_z$  are good quantum numbers and the envelope functions for the effective mass Hamiltonian (26) can be written as

$$\mathcal{F}_{n,v} = \frac{e^{i(k_y y + k_z z)}}{\sqrt{\mathcal{A}}} \begin{bmatrix} a_{n,1,v}(k_z) \phi_{n-1} \\ a_{n,2,v}(k_z) \phi_{n-2} \\ a_{n,3,v}(k_z) \phi_n \\ a_{n,4,v}(k_z) \phi_n \\ a_{n,5,v}(k_z) \phi_n \\ a_{n,6,v}(k_z) \phi_{n+1} \\ a_{n,7,v}(k_z) \phi_{n-1} \\ a_{n,8,v}(k_z) \phi_{n-1} \end{bmatrix}. \quad (27)$$

In Eq. (27),  $n$  is the Landau quantum number associated with the Hamiltonian matrix,  $v$  labels the eigenvectors,  $\mathcal{A} = L_x L_y$  is the cross-sectional area of the sample in the  $xy$  plane,  $\phi_n(\xi)$  are harmonic oscillator eigenfunctions evaluated at  $\xi = x - \lambda^2 k_y$ , and  $a_{n,m,v}(k_z)$  are complex expansion coefficients for the  $v$ th eigenstate which depends explicitly on  $n$  and  $k_z$ . Note that the wave functions themselves will be given by the envelope functions in Eq. (27) with each component multiplied by the corresponding  $k_z=0$  Bloch basis states given in Eqs. (1) and (2).

Substituting  $\mathcal{F}_{n,v}$  from Eq. (27) into the effective mass Schrödinger equation with  $H$  given by Eq. (26), we obtain a matrix eigenvalue equation. By neglecting the second term in  $M$  as described in Eq. (12e),  $H$  is block diagonal in the Landau quantum number  $n$ . We obtain a set of matrix eigenvalue equations

$$H_n F_{n,v} = E_{n,v}(k_z) F_{n,v}, \quad (28)$$

which can be solved separately for each allowed value of the Landau quantum number  $n$  to obtain the Landau levels  $E_{n,\nu}(k_z)$ . The components of the normalized eigenvectors  $F_{n,\nu}$  are the expansion coefficients  $a_i$ .

Since the harmonic oscillator functions  $\phi_{n'}(\xi)$  are only defined for  $n' \geq 0$ , it follows from Eq. (27) that  $F_{n,\nu}$  is defined for  $n \geq -1$ . The energy levels are denoted  $E_{n,\nu}(k_z)$  where  $n$  labels the Landau level and  $\nu$  labels the eigenenergies belonging to the same Landau level in ascending order.

For  $n = -1$ , we set all coefficients  $a_i$  to zero except for  $a_6$  in order to prevent harmonic oscillator eigenfunctions  $\phi_{n'}(\xi)$  with  $n' < 0$  from appearing in the wave function. The eigenfunction in this case is a pure heavy-hole spin-down state and the Hamiltonian is now a  $1 \times 1$  matrix whose eigenvalue corresponds to a heavy-hole spin-down Landau level.

For  $n = 0$ , we must set  $a_1 = a_2 = a_7 = a_8 = 0$  and the Landau levels and envelope functions are then obtained by diagonalizing a  $4 \times 4$  Hamiltonian matrix obtained by striking out the appropriate rows and columns. For  $n = 1$ , the Hamiltonian matrix is  $7 \times 7$  and for  $n \geq 2$  the Hamiltonian matrix is  $8 \times 8$ .

The matrix  $H_n$  in Eq. (28) is the sum of Landau, Zeeman, and exchange contributions. The explicit forms for the Zeeman and exchange Hamiltonian matrices are given in Eqs. (18) and (22) and are independent of  $n$ . The explicit form of the Landau Hamiltonian for an arbitrary value of  $n$  is given in Appendix A.

### C. Analytical solutions using the Kane model

In this section we derive analytical expressions that describe the conduction-band cyclotron resonance energies and  $g$  factors in  $\text{In}_{1-x}\text{Mn}_x\text{As}$ .

#### 1. General formalism

The full Hamiltonian of the problem is given by Eq. (26). The natural way to diagonalize this  $8 \times 8$  matrix analytically is to treat the off-diagonal elements within perturbation theory. This approach, however, remains valid only if the off-diagonal elements are much smaller than the band gap (we are interested in the conduction-band states only). Due to strong  $s$ - $p$  coupling and the relatively small band gap in InAs, this condition breaks down quickly with increasing magnetic field. In fact,  $V\lambda^{-1}$  exceeds the value of one-half of band gap at  $B \approx 25$  T.

Since we are interested in ultrahigh-field cyclotron resonance, we choose another approach similar to that used by Kane.<sup>21</sup> Namely, we neglect the small terms in the Hamiltonian matrix (26) arising from the free-electron kinetic energy and the interaction with remote bands. In other words, we neglect all terms proportional to  $\lambda^{-2}$ . Note that these terms are small compared to the band gap. They are proportional to the magnetic field and are on the order of  $\sim 10$  meV at a field of  $B = 100$  T.

Of course, one of the main drawbacks of the Kane Hamiltonian is that the heavy-hole band is flat (neglecting the free-electron terms) and the Luttinger model, as well as the modified Pidgeon-Brown model discussed above, was devel-

oped to take into account coupling to remote bands, thereby giving the heavy-hole band the correct mass. Since in this work we are only interested in the conduction bands, this approximation is not crucial and it will allow us to obtain analytical expressions for the conduction-band energies.

Our Hamiltonian then is the sum of two parts. The first term is a  $\mathbf{k} \cdot \mathbf{p}$  Hamiltonian that takes into account only the interactions between conduction and valence bands and the second term is the carrier-magnetic ion exchange interaction. Neglecting the second term, solutions of the Hamiltonian can be found analytically. For the second term, even in the limit of saturated  $\langle S_z \rangle$ , the exchange interaction is much smaller than the band gap and, thus, it can be treated as a perturbation even in high magnetic fields. Therefore, as unperturbed states we take the solutions of the Kane-like Hamiltonian and consider the Mn  $s(p)$ - $d$  exchange interaction to first order in perturbation theory.

Solutions of the Kane Hamiltonian can be written in the general form

$$E = \frac{1}{m^*(E)} \left( \mu_B B (2n+1) + \frac{\hbar^2 k_z^2}{2m_0} \right) \pm \frac{1}{2} g^*(E) \mu_B B, \quad (29)$$

where we have introduced an energy-dependent dimensionless effective mass

$$\frac{1}{m^*(E)} = \frac{E_p}{3} \left[ \frac{2}{E + E_g} + \frac{1}{E + E_g + \Delta} \right] \quad (30)$$

and effective  $g$  factor

$$g^*(E) = \frac{2E_p}{3} \left[ \frac{1}{E + E_g + \Delta} - \frac{1}{E + E_g} \right]. \quad (31)$$

Note that we have neglected the free-electron contributions to these terms. The upper and lower signs in Eq. (29) correspond to spin-up and spin-down conduction-band states, respectively, and the zero of energy is chosen to lie at the bottom of the conduction band when  $B = 0$ .

Note also, for this section only, that we have redefined the index  $n$  compared to the full model which was discussed in the previous section. In Eq. (29) for electron spin up we follow Pidgeon and Brown<sup>11</sup> and redefine the Landau quantum number  $n$  by making the transformation  $n \rightarrow n + 1$  so that  $n = 0$  corresponds to the ground-state Landau level for both spin-up and spin-down solutions. While this convention on the numbering of  $n$  is convenient for discussing the Landau levels in the conduction band, it can be applied only for states in the simplified Kane Hamiltonian. For the more general model where the index  $n$  ranges from  $-1$  to  $\infty$ , the lowest spin-up conduction Landau level is in the  $n = 1$  manifold and the lowest-lying spin-down level is in the  $n = 0$  manifold. Thus, our use of the Pidgeon and Brown labeling convention for  $n$  is confined to this section only.

Once solutions of Eq. (29) are known, the first-order perturbative correction due to the carrier-magnetic ion  $s(p)$ - $d$  exchange interaction is given by

$$E^{(1)} = \pm \bar{x} N \left( \alpha + \beta \mu_B B \frac{E_p}{9} \left[ \frac{8n+4 \mp 5}{(E+E_g)^2} + \frac{2n+1 \pm 1}{(E+E_g+\Delta)^2} + \frac{8n+4 \pm 4}{(E+E_g)(E+E_g+\Delta)} \right] + \beta \frac{\hbar^2 k_z^2}{2m_0} \frac{E_p}{9} \left[ \frac{2}{(E+E_g)^2} - \frac{1}{(E+E_g+\Delta)^2} + \frac{8}{(E+E_g)(E+E_g+\Delta)} \right] \right), \quad (32)$$

with

$$N = \left( 1 + \mu_B B \frac{E_p}{3} \left[ \frac{4n+2 \mp 1}{(E+E_g)^2} + \frac{2n+1 \pm 1}{(E+E_g+\Delta)^2} \right] + \frac{\hbar^2 k_z^2}{2m_0} \frac{E_p}{9} \left[ \frac{2}{(E+E_g)^2} + \frac{1}{(E+E_g+\Delta)^2} \right] \right)^{-1}, \quad (33)$$

where we introduce the notation  $\bar{x} = x N_0 \langle S_z \rangle / 2$ . Upper and lower signs again correspond to spin-up and spin-down conduction-band states, respectively.

Note that from Eq. (32) we can immediately gain some insight into the effects of the  $s(p)$ - $d$  exchange interaction on the narrow-gap material. (i) Since we do not take into account variation of the material parameters (such as the energy gap) with manganese concentration  $x$ , it follows immediately from Eq. (32) that we obtain a linear dependence of the conduction-band energies on  $x$ . (ii) Without conduction-valence-band mixing, the first-order correction would be  $E^{(1)} = \pm \bar{x} N \alpha$  as one might expect. (In this case, there would be no shift in the cyclotron resonance energy with Mn doping  $x$  since all levels for a given spin would be shifted by the same amount.) The term proportional to  $\beta$  is a direct consequence of conduction-valence band mixing. (iii) It is also seen from Eq. (32) that both band mixing contributions induced by the magnetic field  $B$  and motion in the  $z$  direction ( $k_z$ ) have the same sign and, since  $\alpha$  and  $\beta$  are of opposite signs, both reduce  $E^{(1)}$ .

To calculate the conduction band energy spectrum using Eqs. (32) and (33) we need to know the energies of the unperturbed problem. In spite of its clear form, Eq. (29) is indeed a third-order equation and its general solutions are quite complicated. Standard approximations usually assume either strong spin-orbit interaction ( $\Delta \gg E_g + E$ ) (Ref. 22) or small kinetic energy ( $E \ll E_g + \Delta$ ) (Ref. 23). In the present paper we are interested in strong magnetic fields where  $E \sim E_g \approx \Delta$  and have to use the general solution. However, in our situation we can make one more simplification, suitable for the particular case of InAs-based semiconductors. Using the fact that in InAs the energy gap is approximately equal to the spin-orbit splitting, we set  $E_g = \Delta$ . Although this approximation is not necessary to obtain analytical solutions, it makes the final expressions more readable.

With these simplifications solutions of Eq. (29)—i.e., energies of unperturbed states in our model—can be presented as

$$E^{(0)} \approx E_0 + T_z, \quad (34)$$

with

$$T_z = \frac{1}{m^*(E_0)} \frac{\hbar^2 k_z^2}{2m_0}. \quad (35)$$

The position of the bottom of the Landau subbands has the form

$$E_0 = 2 \sqrt{\frac{\Delta^2 + (2n+1)V'^2}{3}} \times \cos \left[ \frac{1}{3} \arccos \left( \frac{\sqrt{3}(4n+2 \mp 1)\Delta V'^2}{2\sqrt{[\Delta^2 + (2n+1)V'^2]^3}} \right) \right] - \Delta, \quad (36)$$

where the upper (lower) sign corresponds to electron spin-up (-down) states. In Eq. (36) we have introduced  $V' \equiv V\lambda^{-1} = \sqrt{\mu_B B E_p}$ .

The second term in Eq. (34) is the kinetic energy for the motion along the magnetic field. It assumes parabolic dispersion with the effective masses being different for each Landau subband. This approximation is valid near the bottom of the Landau subbands and is justified when  $T_z \ll E_g + E_0$ .

Equations (32)–(36) fully describe, within the Kane model, the conduction-band energy spectra of  $\text{In}_{1-x}\text{Mn}_x\text{As}$  in a magnetic field. From the energy spectra one can easily calculate different physical quantities observed in cyclotron resonance experiments, such as cyclotron masses or  $g$  factors. However, the general expressions are rather complicated for direct analysis, but can be significantly simplified in the limits of low ( $V' \ll \Delta$ ) and high ( $V' \gg \Delta$ ) magnetic fields. First we consider the situation at the bottom of the Landau subbands. Then we take into account finite  $k_z$ .

## 2. Low-field and high-field limits

The cyclotron energies are defined as the splitting between the two lowest Landau levels ( $n=0$  and  $n=1$ ) and are given by  $\Delta E \equiv E(n=1) - E(n=0)$ .

The low-magnetic-field limit of the cyclotron energies can be obtained by expanding to second order in powers of  $V'/\Delta \ll 1$ . The result for spin-up states is

$$\Delta E_{\uparrow} \approx \Delta \frac{5}{3} \frac{V'^2}{\Delta^2} - \bar{x}(\alpha - \beta) \frac{3}{2} \frac{V'^2}{\Delta^2} - \bar{x}\beta \frac{1}{9} \frac{V'^2}{\Delta^2}, \quad (37)$$

and for spin-down states we obtain

$$\Delta E_{\downarrow} \approx \Delta \frac{5}{3} \frac{V'^2}{\Delta^2} + \bar{x}(\alpha - \beta) \frac{3}{2} \frac{V'^2}{\Delta^2} + \bar{x}\beta \frac{1}{9} \frac{V'^2}{\Delta^2}. \quad (38)$$

It is seen that in small magnetic fields the cyclotron energy splitting increases linearly with the field that corresponds to simple parabolic dispersions at small  $k$ .

Likewise, the cyclotron energy in the high-magnetic-field limit is obtained by expanding the energy splitting to second order in  $\Delta/V' \ll 1$ . The results are

$$\Delta E_{\uparrow} \approx V' \left( \sqrt{3} - 1 + \frac{1}{9} \frac{\Delta}{V'} - 0.24 \frac{\Delta^2}{V'^2} \right) - \bar{x}(\alpha - \beta) 0.21 \frac{\Delta}{V'} \quad (39)$$

for spin up and

$$\Delta E_{\downarrow} \approx V' \left( \sqrt{3} - 1 - \frac{1}{9} \frac{\Delta}{V'} + 0.03 \frac{\Delta^2}{V'^2} \right) + \bar{x}(\alpha - \beta) 0.07 \frac{\Delta}{V'} \quad (40)$$

for spin down. At high magnetic fields, nonparabolicity due to conduction and valence-band mixing results in a square-root dependence of the cyclotron energy on magnetic field.<sup>22,24–26</sup>

It is also seen from Eqs. (37)–(40) that the electron energy mainly depends not on two independent exchange constants  $\alpha$  and  $\beta$ , but on their difference  $(\alpha - \beta)$ . This feature will be discussed in more detail in Sec. IV D.

It is also easy to obtain limiting expressions for the spin splitting of the conduction-band states. For the lowest Landau sublevels this spin splitting  $\Delta E_0 \equiv E_{\uparrow}(n=0) - E_{\downarrow}(n=0)$  is

$$\Delta E_0 \approx -\frac{\Delta}{3} \frac{V'^2}{\Delta^2} + 2\bar{x}\alpha - \bar{x}(\alpha - \beta) \frac{3}{2} \frac{V'^2}{\Delta^2} - \bar{x}\beta \frac{1}{9} \frac{V'^2}{\Delta^2} \quad (41)$$

in the low-magnetic-field limit and

$$\Delta E_0 \approx -\frac{\Delta}{3} \left( 1 - \frac{\Delta}{V'} \right) + \bar{x}(\alpha + \beta) + \bar{x} \frac{2}{3} \frac{\Delta}{V'} (\alpha - \beta) \quad (42)$$

in the high-field limit. The first term in Eq. (41) corresponds to a well-known low-field negative contribution to the electron  $g$  factor due to the influence of the spin-orbit split valence bands  $\Gamma_8$  and  $\Gamma_7$  (Ref. 27) and can be obtained by putting  $E_g = \Delta$  in the conventional expression of Eq. (31). The second term in Eq. (41) is opposite in sign and describes a contribution due to the  $s$ - $d$  exchange interaction. This term dominates in low magnetic fields and is responsible for the giant spin splitting of the conduction bands observed in diluted magnetic semiconductors. With increasing magnetic field  $\langle S_z \rangle$  quickly saturates and the first term in Eq. (41) becomes dominant. Under certain conditions this may result in a change of the sign of the spin splitting. If we go beyond the low-field limit, the first term in Eq. (41) ceases to be linear in the magnetic field and, finally, saturates to  $-\Delta/3$  in the high-field limit, as seen in Eq. (42). At the same time,

since exchange constants  $\alpha$  and  $\beta$  have the opposite signs, strong valence-conduction-band mixing results in a reduction of the exchange-induced spin splitting of the conduction-band and a term  $\bar{x}(\alpha + \beta)$  appears in Eq. (42) instead of  $2\bar{x}\alpha$  in Eq. (41).

Finally, let us note that the spin splitting is different for different Landau sublevels. For example, for the first excited Landau sublevels (with  $n=1$ ) the expressions analogous to Eqs. (41) and (42) have the form

$$\Delta E_1 \approx -\frac{\Delta}{3} \frac{V'^2}{\Delta^2} + 2\bar{x}\alpha - \bar{x}(\alpha - \beta) \frac{9}{2} \frac{V'^2}{\Delta^2} - \bar{x}\beta \frac{1}{3} \frac{V'^2}{\Delta^2} \quad (43)$$

in the low-field limit and

$$\Delta E_1 \approx -\frac{\Delta}{9} \left( 1 - \frac{1}{\sqrt{3}} \frac{\Delta}{V'} \right) + \bar{x}(\alpha + \beta) + \bar{x} \frac{2}{3\sqrt{3}} \frac{\Delta}{V'} (\alpha - \beta) \quad (44)$$

in the high-field limit. There are two reasons for this behavior. First, with increasing  $n$  the energy separation between conduction- and valence-band states increases and this suppresses the influence of the valence band on the electron  $g$  factor. As a result, in the high-field limit, the corresponding term saturates to  $-\Delta/9$ , which is 3 times smaller than for Landau sublevels with  $n=0$ . Second, the Landau quantum number  $n$  affects the degree of conduction-valence-band mixing, resulting in a dependence of the exchange interaction contribution to the  $g$  factor on  $n$ .

### 3. Finite $k_z$

The main physics associated with finite  $k_z$  is the presence of additional conduction-valence-band mixing induced by free motion along the magnetic field. This effect is most pronounced if we consider low-field spin splitting of the conduction-band states. Expanding the corresponding expressions to first order in powers of  $T_0/\Delta \ll 1$  [ $T_0$  is the kinetic energy (35) with conduction-band edge effective mass] we find that the term

$$\Delta E_0^{k_z} \approx -\bar{x} \frac{9}{5} (\alpha - \beta) \frac{T_0}{\Delta} - \bar{x} \frac{4}{15} \beta \frac{T_0}{\Delta} \quad (45)$$

should be added to Eq. (41) in the general case of states with  $k_z \neq 0$ . The last two terms in Eq. (41) together with Eq. (45) describe the influence of the  $s$ - $p$  coupling on the spin splitting of the conduction band Landau subbands. It is worth noting that both these contributions lead to a reduction of the  $s$ - $d$  exchange splitting  $2\bar{x}\alpha$ . Let us also note the difference in their manifestation. Magnetic-field-induced  $s$ - $p$  mixing becomes pronounced at relatively strong magnetic fields. At such fields, however, the role of exchange interaction is decreased by the conventional spin splitting [first term in Eq. (41)]. At the same time, the  $k_z$ -induced contribution could be important even in small magnetic fields, when the exchange interaction plays the dominant role in spin splitting of conduction-band states.

In our model, exchange interaction is considered within first-order perturbation theory. As a result, all physical quantities like  $g$  factors or cyclotron masses are linear functions of the manganese concentration  $x$ . This means, in particular, that if the exchange interaction contribution to the spin splitting vanishes for a certain concentration of magnetic ions, it should vanish at the same  $k_z$ , magnetic field, and temperature for any value of  $x$ . The results of numerical diagonalization of the full Hamiltonian matrix (26) (presented in Fig. 5) support this conclusion and justify our model.

#### D. Magneto-optical absorption

In this section, we discuss how we calculate the magneto-optical properties. We calculate the magneto-optical absorption coefficient at the photon energy  $\hbar\omega$  from<sup>28</sup>

$$\alpha(\hbar\omega) = \frac{\hbar\omega}{(\hbar c)n_r} \epsilon_2(\hbar\omega), \quad (46)$$

where  $\epsilon_2(\hbar\omega)$  is the imaginary part of the dielectric function and  $n_r$  is the index of refraction. The imaginary part of the dielectric function is found using Fermi's golden rule. The result is

$$\begin{aligned} \epsilon_2(\hbar\omega) = & \frac{e^2}{\lambda^2(\hbar\omega)^2} \sum_{n,\nu;n',\nu'} \int_{-\infty}^{\infty} dk_z |\hat{e} \cdot \vec{P}_{n,\nu}^{n',\nu'}(k_z)|^2 \\ & \times [f_{n,\nu}(k_z) - f_{n',\nu'}(k_z)] \delta(\Delta E_{n,\nu}^{n',\nu'}(k_z) - \hbar\omega), \end{aligned} \quad (47)$$

where  $\Delta E_{n,\nu}^{n',\nu'}(k_z) = E_{n',\nu'}(k_z) - E_{n,\nu}(k_z)$  is the transition energy. The function  $f_{n,\nu}(k_z)$  in Eq. (47) is the probability that the state  $(n, \nu, k_z)$ , with energy  $E_{n,\nu}(k_z)$ , is occupied. It is given by the Fermi distribution function

$$f_{n,\nu}(k_z) = \frac{1}{1 + \exp[(E_{n,\nu}(k_z) - E_f)/kT]}. \quad (48)$$

The Fermi energy  $E_f$  in Eq. (48) depends on temperature and doping. If  $N_D$  is the donor concentration and  $N_A$  the acceptor concentration, then the net donor concentration  $N_C = N_D - N_A$  can be either positive or negative depending on whether the sample is  $n$  or  $p$  type. For a fixed temperature and Fermi level, the net donor concentration is

$$N_C = \frac{1}{(2\pi)^2 \lambda^2} \sum_{n,\nu} \int_{-\infty}^{\infty} dk_z [f_{n,\nu}(k_z) - \delta_{n,\nu}^v], \quad (49)$$

where  $\delta_{n,\nu}^v = 1$  if the subband  $(n, \nu)$  is a valence band and vanishes if  $(n, \nu)$  is a conduction band. Given the net donor concentration and the temperature, the Fermi energy can be found from Eq. (49) using a root finding routine.

Since the envelope functions and vector potential are slowly varying over a unit cell, the dominant contributions to the optical matrix elements are given by

TABLE II. Material parameters for  $\text{In}_{1-x}\text{Mn}_x\text{As}$ .

Energy gap (eV) <sup>a</sup>	
$E_g(T=30\text{ K})$	0.415
$E_g(T=290\text{ K})$	0.356
Electron effective mass ( $m_0$ )	
$m_e^*$	0.022
Luttinger parameters <sup>b</sup>	
$\gamma_1^L$	20.0
$\gamma_2^L$	8.5
$\gamma_3^L$	9.2
$\kappa^L$	7.53
Spin-orbit splitting (eV) <sup>b</sup>	
$\Delta$	0.39
Mn $s$ - $d$ and $p$ - $d$ exchange energies (eV)	
$N_0 \alpha$	-0.5
$N_0 \beta$	1.0
Optical matrix parameter (eV) <sup>b</sup>	
$E_p$	21.5
Refractive index <sup>c</sup>	
$n_r$	3.42

<sup>a</sup>Equation (51) with parameters from Ref. 14.

<sup>b</sup>Reference 14.

<sup>c</sup>Reference 31.

$$\begin{aligned} \hat{e} \cdot \vec{P}_{n,\nu}^{n',\nu'}(k_z) = & \sum_{m,m'} a_{n,m,\mu}^*(k_z) a_{n',m',\mu'}(k_z) \\ & \times \langle \phi_{N(n,m)} | \phi_{N(n',m')} \rangle \langle m | (\hat{e} \cdot \vec{P}) | m' \rangle, \end{aligned} \quad (50)$$

where  $\hat{e}$  is the unit polarization vector of the radiation,  $a_{n,m,\mu}(k_z)$  are the complex expansion coefficients for the envelope functions in Eq. (27), and  $\phi_{N(n,m)}$  are orthonormalized harmonic oscillator wave functions. Their quantum numbers  $N(n,m)$  depend explicitly on  $n$  and  $m$  as defined in Eq. (27). In Eq. (50), we have neglected a term that depends on the momentum matrix element  $\langle \phi_{N(n,m)} | (\hat{e} \cdot \vec{P}) | \phi_{N(n',m')} \rangle$  between the oscillator states. Owing to strong band mixing in the narrow-gap materials, this term is much smaller than the momentum matrix elements between the Bloch basis functions, *even for intraband optical absorption* such as for cyclotron resonance; hence we neglect it.

The momentum matrix elements  $\langle m | P_x | m' \rangle$ ,  $\langle m | P_y | m' \rangle$ , and  $\langle m | P_z | m' \rangle$  are the momentum matrix elements between the Bloch basis functions  $|m\rangle$  defined in Eqs. (1) and (2). Explicit expressions for the momentum matrices  $P_x$ ,  $P_y$ , and  $P_z$  are found in Appendix B.

In our simulations, we consider  $e$ -active circularly polarized light incident along the  $z$  axis. For  $e$ -active circular polarization, the unit polarization vector is  $\hat{e} = (\hat{x} - i\hat{y})/\sqrt{2}$ . In performing the integral in Eq. (47) the Dirac delta function  $\delta(x)$  in Fermi's golden rule is replaced by the Lorentzian line shape function  $\Delta_\gamma(x)$  with full width at half maximum (FWHM) of  $\gamma$ .

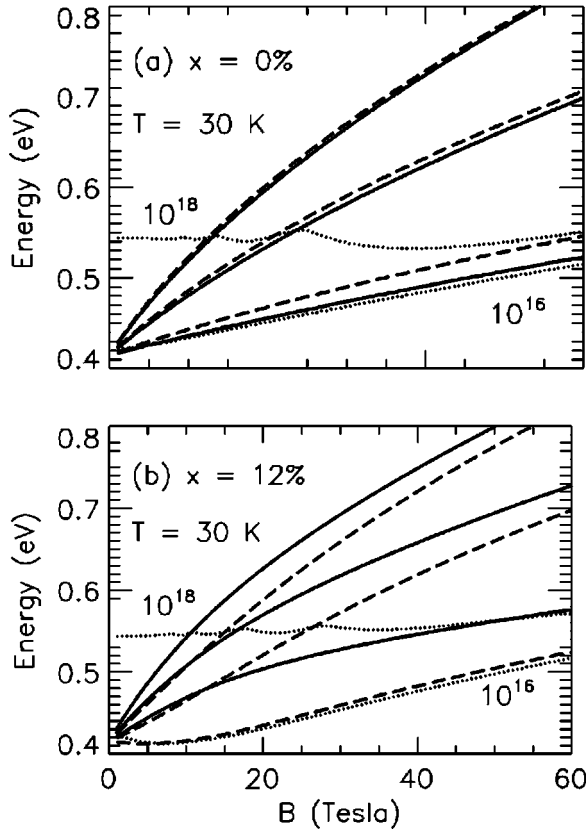


FIG. 3. Zone-center Landau conduction-subband energies at  $T = 30$  K as functions of magnetic field in  $n$ -doped  $\text{In}_{1-x}\text{Mn}_x\text{As}$  for (a)  $x=0\%$  and (b)  $x=12\%$ . Solid lines are spin-up and dashed lines are spin-down levels. The Fermi energies are shown as dotted lines for  $n = 10^{16}\text{cm}^{-3}$  and  $n = 10^{18}\text{cm}^{-3}$ .

### E. Material parameters

The material parameters we use are shown in Table II. For the temperature-dependent energy gap  $E_g$  of InAs we use the empirical Varshni formula<sup>14,29</sup>

$$E_g = E_0 - \frac{aT^2}{T+b}, \quad (51)$$

with  $E_0 = 0.417$  eV,  $a = 2.76 \times 10^{-4}$  eV/K, and  $b = 93$  K. As seen in Table I, the experimental cyclotron mass does not vary significantly with temperature. Other low-field CR studies of InAs (Ref. 30) also show a very weak temperature dependence of the cyclotron mass. To account for a mass that only slightly varies with temperature, we keep the mass constant with temperature and adjust the  $\gamma_4$  parameter [Eq. (16)] to account for the temperature-dependent band gap. Alternatively, one might wish to keep  $\gamma_4$  constant and vary the  $\mathbf{k} \cdot \mathbf{p}$  optical matrix element  $E_p$ .

## IV. RESULTS

### A. Landau levels and $g$ factors

In Fig. 3(a), the six lowest-lying zone-center ( $k_z = 0$ ) Landau conduction-subband energies in InAs are shown as functions of applied magnetic field. At  $k_z = 0$ , the submatrix  $L_c$  in

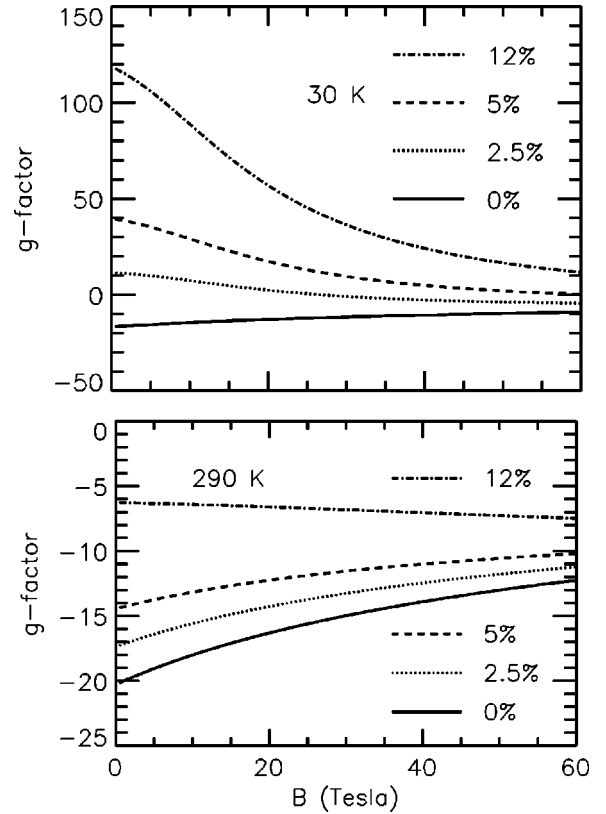


FIG. 4. Gyromagnetic factors at  $k=0$  for the lowest Landau subband in  $n$ -type  $\text{In}_{1-x}\text{Mn}_x\text{As}$  as a function of applied magnetic field for several values of the Mn concentration  $x$ . The upper panel is for  $T=30$  K and the lower panel is for  $T=290$  K.

the Landau Hamiltonian  $H_L$  vanishes identically and the Hamiltonian  $H$  in Eq. (26) is block diagonal with respect to the upper and lower Bloch basis states in Eqs. (1) and (2). In Fig. 3 the spin-up Landau levels are shown as solid lines while spin-down Landau levels are shown as dashed lines. The Fermi energies for two different electron concentrations  $n = 10^{16}\text{cm}^{-3}$  and  $n = 10^{18}\text{cm}^{-3}$  are shown as dotted lines. At a concentration of  $n = 10^{16}\text{cm}^{-3}$ , only the lowest Landau subband is occupied at  $B = 60$  T, while at  $n = 10^{18}\text{cm}^{-3}$ , the first two Landau subbands are occupied.

In the absence of Mn impurities, it is well known that at low magnetic fields, the spin splittings between the electron spin-up and spin-down Landau levels, at the band edge, can be described in terms of an effective gyromagnetic factor<sup>27,32</sup>

$$g^* = 2 \left( 1 - \frac{E_p}{3E_g} \frac{\Delta}{E_g + \Delta} \right). \quad (52)$$

This is just Eq. (31) with  $E=0$  and the bare  $g$  factor 2 included. The  $g$  factor in Eq. (52) depends on temperature through the temperature-dependent band gap. For bulk InAs at  $T=30$  K we find  $g^* = -14.7$  and for  $T=290$  K we have  $g^* = -19.0$ . At nonzero magnetic fields, the expression for the gyromagnetic factor in Eq. (52) is not correct. As a function of the magnetic field, the spin splittings become nonlinear as seen in Fig. 3(a) and depend explicitly on the Landau

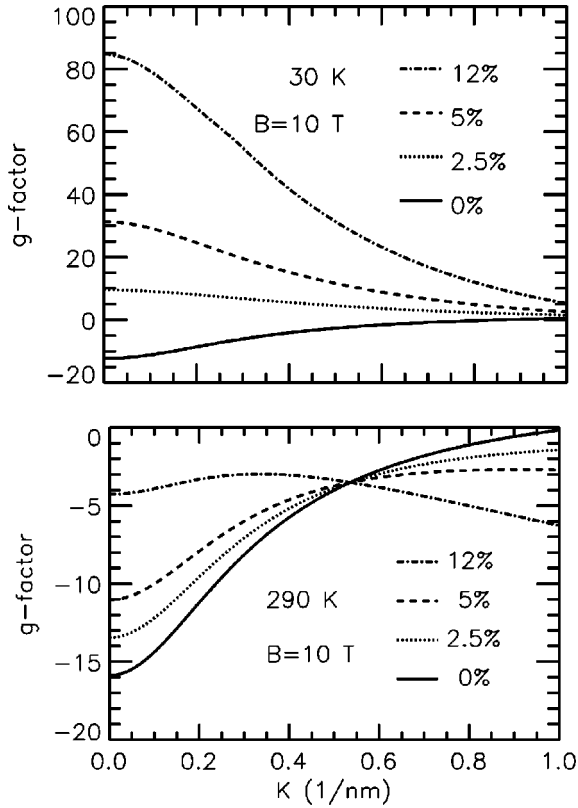


FIG. 5. Gyromagnetic factors at  $B=10$  Tesla for the lowest Landau subband in  $n$ -type  $\text{In}_{1-x}\text{Mn}_x\text{As}$  as a function of  $k$ .  $g$  factors for several values of Mn concentration are shown. The upper panel is for  $T=30$  K and the lower panel is for  $T=290$  K.

subband level indices  $n$ . This results from the nonparabolicity in the narrow-gap material.

The effect of doping InAs with Mn is shown in Fig. 3(b) where the Landau subband levels for  $\text{In}_{0.88}\text{Mn}_{0.12}\text{As}$  are plotted. At low fields, the effect of doping with Mn is to alter the gyromagnetic factor. The gyromagnetic factor in the presence of Mn impurities is<sup>32</sup>

$$g_{Mn}^* = g^* + \frac{xN_0\alpha\langle S_z \rangle}{\mu_B B}. \quad (53)$$

Since the sign of  $\alpha$  is negative, the gyromagnetic factor increases with the applied magnetic field. At sufficiently high Mn concentrations and magnetic fields, the low-temperature gyromagnetic factor can become positive and the spin splittings reverse as seen in Fig. 3(b).

We have examined the electron  $g$  factors for the lowest spin-down and spin-up Landau levels with energies  $E_{0,4}(k_z)$  and  $E_{1,6}(k_z)$ , respectively. The gyromagnetic factor is obtained by diagonalizing the Hamiltonians  $H_0$  and  $H_1$  in the matrix eigenvalue problem (28) and computing the gyromagnetic factor as

$$g = \frac{E_{0,4}(k_z) - E_{1,6}(k_z)}{\mu_B B}. \quad (54)$$

The gyromagnetic factor can depend on the temperature, the magnetic field, and the wave vector.

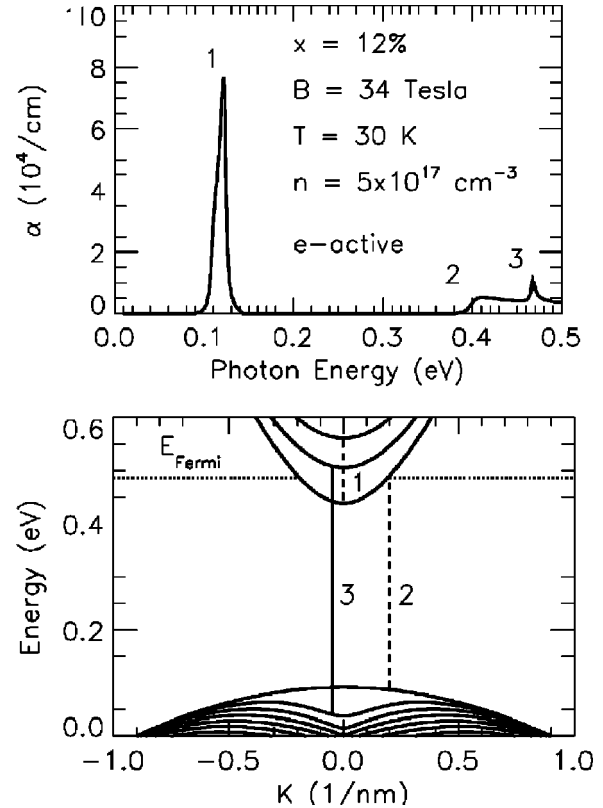


FIG. 6. The upper panel shows the absorption spectrum for  $n$ -doped  $\text{In}_{0.88}\text{Mn}_{0.12}\text{As}$  in a magnetic field. The radiation is  $e$ -circularly polarized and the FWHM is taken to be 4 meV. The bandstructure and Fermi energy are shown in the lower panel. Three vertical transitions labeled 1, 2, and 3 correspond to absorption features in the upper panel. Transitions between spin-up levels are shown as solid lines and transitions between spin-down levels are shown as dashed lines.

In Fig. 4 the gyromagnetic factor for the zone center is plotted as a function of the magnetic field for two different temperatures and four different values of the Mn concentration. In all cases, doping with Mn impurities is seen to increase the  $g$  factor and the effect is seen to be sensitive to both the temperature and the Mn concentration. The sensitivity to temperature and Mn concentration arises from the factor  $x\langle S_z \rangle$  in the Mn exchange Hamiltonian (22). In the paramagnetic phase,  $\langle S_z \rangle$  is related to the temperature and magnetic field in accordance with the simple Brillouin function expression of Eq. (24).

In Fig. 5, the gyromagnetic factor is plotted as a function of the wavevector  $k_z$  for a magnetic field of  $B=10$  T. As in Fig. 4, two temperatures and four Mn concentrations are considered. We note that in Fig. 5(b) all the curves cross around  $k_z \approx 0.5 \text{ nm}^{-1}$ , indicating that the exchange interaction contribution to the  $g$  factor vanishes for this state regardless of the Mn concentration. The reason for this curious situation was explained earlier in our discussion of the Kane model.

## B. Magnetoabsorption

The magnetoabsorption spectrum and band structure for  $n$ -doped  $\text{In}_{1-x}\text{Mn}_x\text{As}$  are shown in the upper and lower pan-

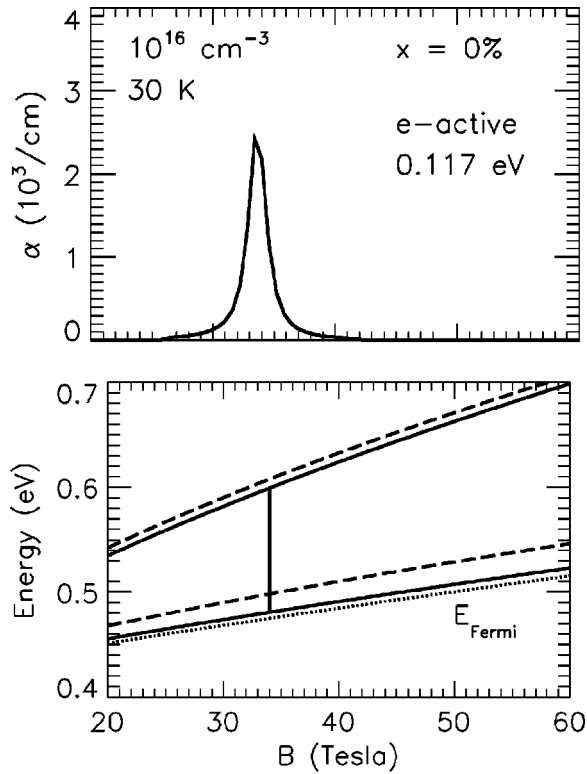


FIG. 7. The upper panel shows the cyclotron absorption as a function of magnetic field in *n*-type InAs. The radiation is *e*-active circularly polarized with  $\hbar\omega = 0.117 \text{ eV}$ . The FWHM linewidth is taken to be 4 meV. The lower panel shows the four lowest conduction Landau levels and the Fermi energy as a function of applied magnetic field. Solid lines are spin-up levels and dashed lines are spin-down levels.

els of Fig. 6 for *e*-active circular polarization. In our simulation, the Mn concentration is  $x = 12\%$ , the external magnetic field  $B = 34 \text{ T}$ , the carrier concentration  $n = 5 \times 10^{17} \text{ cm}^{-3}$ , and the temperature  $T = 30 \text{ K}$ . The FWHM is taken to be 4 meV in our calculation. In the bottom panel of Fig. 6 the Landau subbands are plotted as a function of wave vector  $k_z$  parallel to the applied magnetic field. The Landau subband energies depend only on  $k_z$  and the band structure is one dimensional. The Fermi energy is indicated by the dotted line, and at this carrier concentration and temperature, only the lowest-lying spin-down conduction subband is populated near the zone center. Electrons in this partially filled subband can be excited to higher-lying conduction subbands. A strong  $\Delta n = 1$  transition (labeled 1) is observed between the filled ground-state conduction subband and the first-excited spin-down conduction subband. Since these two Landau levels have the same curvature, a sharply peaked joint density of states results in the sharp peak in magnetoabsorption observed at a photon energy  $\hbar\omega = 0.117 \text{ eV}$ . Two valence-to-conduction absorption features (labeled 2 and 3) are seen for  $\hbar\omega < 0.5 \text{ eV}$ . Transitions between the ground-state spin-down valence and conduction subbands give rise to the feature labeled 2 in the figure. The band edge for this absorption feature depends on the position of the Fermi energy due to Fermi blocking effects. Another valence-to-conduction sub-

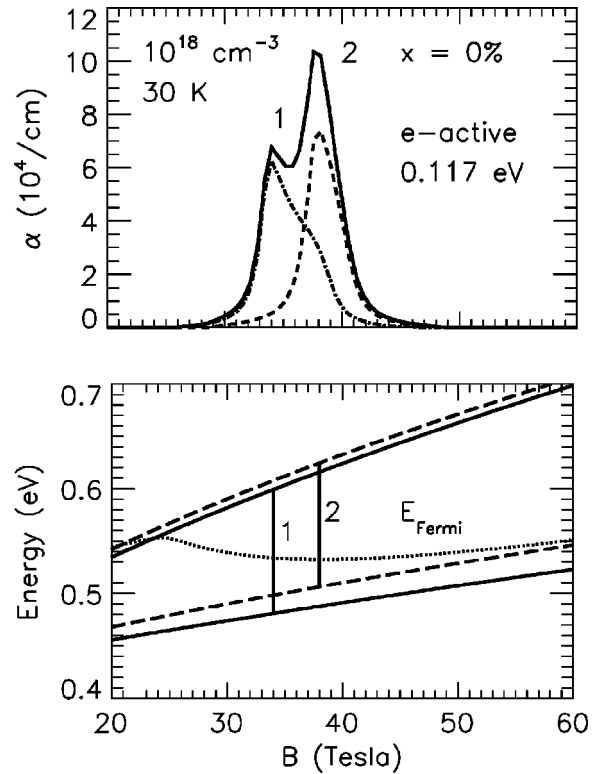


FIG. 8. Same simulation as in Fig. 7 but with the doping density raised to  $n = 10^{18} \text{ cm}^{-3}$ . Since the two lowest Landau levels are occupied, there are now two cyclotron absorption peaks. Peak 1 is the spin-up transition and peak 2 is an additional spin-down transition. The dash-dotted and dashed lines show the individual contributions to the cyclotron resonance absorption from transitions 1 and 2, respectively. The asymmetry of the line shape results from the  $k_z \neq 0$  contributions as well as the nonparabolicity.

band transition (labeled 3) is due to transitions between the ground-state spin-up valence and conduction subbands. The valence subband has a characteristic camel back structure and near the zone center has the same curvature as the conduction subband. This results in an enhancement in the joint density of states near the zone center and gives rise to the peak in the absorption spectrum near  $\hbar\omega = 0.47 \text{ eV}$ .

### C. Cyclotron resonance

In Fig. 7, we simulate cyclotron resonance experiments in *n*-type InAs for *e*-active circularly polarized light with photon energy  $\hbar\omega = 0.117 \text{ eV}$ . We assume a temperature  $T = 30 \text{ K}$  and a carrier concentration  $n = 10^{16} \text{ cm}^{-3}$ . The lower panel of Fig. 7 shows the four lowest zone-center Landau conduction-subband energies and the Fermi energy as functions of the applied magnetic field. The transition at the resonance energy  $\hbar\omega = 0.117 \text{ eV}$  is a spin-up  $\Delta n = 1$  transition and is indicated by the vertical line. From the Landau level diagram the resonance magnetic field is found to be  $B = 34 \text{ T}$ . The upper panel of Fig. 7 shows the resulting cyclotron resonance absorption assuming a FWHM linewidth of 4 meV. There is only one resonance line in the cyclotron absorption because only the ground-state Landau level is occupied at low electron densities.

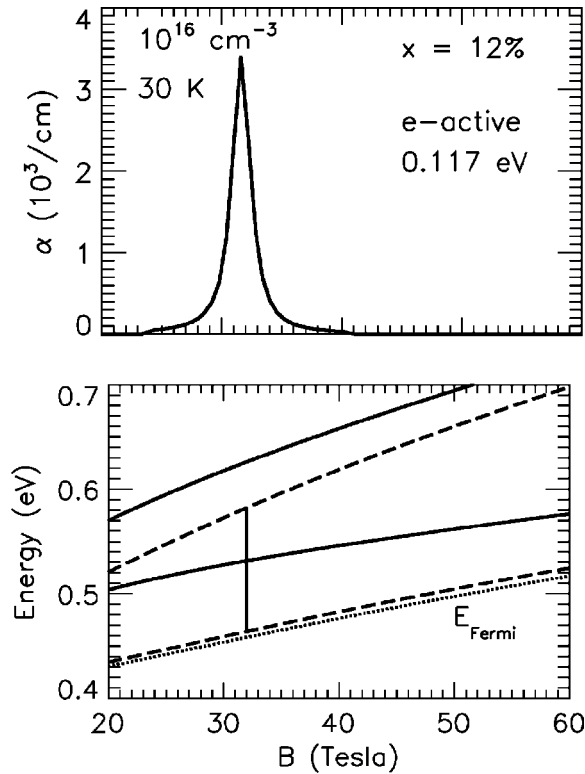


FIG. 9. Same simulation as in Fig. 7 but with the manganese concentration increased to  $x=12\%$ . The cyclotron absorption peak near 32 T is now a spin down  $\Delta n=1$  transition.

At higher electron densities multiple lines can appear in the cyclotron absorption as higher-lying Landau subbands are populated. This is the spin splitting of the cyclotron resonance peaks. This is illustrated in Fig. 8 where the electron density  $n$  has been increased to  $10^{18} \text{ cm}^{-3}$ . We can see in Fig. 8 that both the lowest-lying spin-up and spin-down Landau levels are occupied and that two resonance transitions (labeled 1 and 2 in Fig. 8) result. In addition, we also see that the spin-down peak which comes in at higher electron densities appears to dominate the spin-up peak. This is somewhat misleading. The dash-dotted and dashed lines show the contributions to the cyclotron resonance absorption from transitions 1 and 2, respectively. Both transitions have roughly the same strength, but the line shape for transition 1 is highly asymmetric. This results from taking into account the contributions to the absorption for  $k_z \neq 0$  and also the nonparabolicity of the bands. The line shape for transition 2 is not as asymmetric since the Fermi energy lies closer to the Landau level edge for this transition. Note that if there is substantial scattering so that the transition lines are broadened, then the two transition will be merged into one and can lead to an apparent shift of cyclotron resonance features to higher fields.

The effect on the cyclotron resonance absorption of doping InAs with 12% Mn is shown in Fig. 9. Comparing Figs. 7 and 9, we see that the effect of heavily doping with Mn while keeping the electron concentration  $n$  fixed is to reverse the spin splitting and hence the character and position of the cyclotron absorption peak. The cyclotron absorption peak

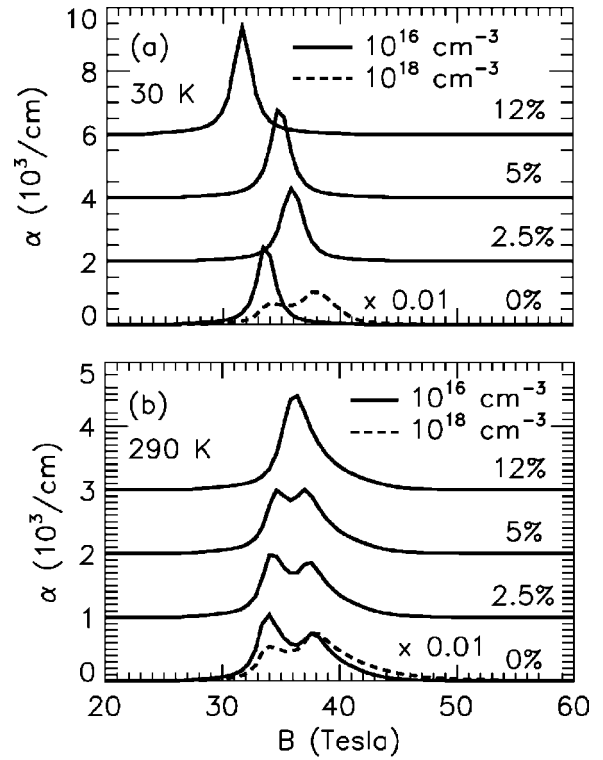


FIG. 10. Cyclotron absorption as a function of magnetic field in  $n$ -doped  $\text{In}_{1-x}\text{Mn}_x\text{As}$  with  $x=0\%$ , 2.5%, 5%, and 12% for (a)  $T=30 \text{ K}$  and (b)  $T=290 \text{ K}$ . The radiation is  $e$ -active circularly polarized with  $\hbar\omega=0.117 \text{ eV}$ .

seen in Fig. 9 is a spin-down transition as opposed to a spin-up transition and the cyclotron resonance peak is seen to shift from  $B=34 \text{ T}$  to  $B=32 \text{ T}$ .

In Fig. 10, we examine more closely the effects of the Mn doping concentration  $x$  on the cyclotron absorption spectra of  $n$ -doped  $\text{In}_{1-x}\text{Mn}_x\text{As}$  for  $e$ -active circularly polarized radiation with photon energy  $\hbar\omega=0.117 \text{ eV}$ . We plot the cyclotron absorption as a function of applied magnetic field for  $x=0\%$ , 2.5%, 5%, and 12%. In all cases we assume a fairly narrow FWHM linewidth of 4 meV. In Fig. 10(a) we plot the cyclotron absorption at  $T=30 \text{ K}$ . All the solid curves are computed for an electron concentration  $n=10^{16} \text{ cm}^{-3}$  and are vertically offset for clarity. For  $x=0\%$ , we plot the cyclotron absorption for  $n=10^{18} \text{ cm}^{-3}$  as a dashed line scaled by a factor of 0.01. In Fig. 10(a), the cyclotron absorption curves for  $x=0\%$  and  $x=12\%$  have already been discussed in Figs. 7, 8, and 9. As  $x$  increases from 0% to 12%, the cyclotron absorption peak initially shifts to higher fields and is due to a  $\Delta n=1$  spin-up transition from the occupied lowest Landau level. At a critical value of the Mn concentration, the spin splittings reverse and the observed transition is now due to a  $\Delta n=1$  spin-down transition. Consequently, the cyclotron absorption begins to decrease with increasing Mn concentration.

To examine the temperature dependence, we also computed the cyclotron absorption at room temperature for several values of  $x$ . The curves in Fig. 10(b) are the same as those in Fig. 10(a) except that the temperature has been increased from  $T=30 \text{ K}$  to  $T=290 \text{ K}$ . We see that the single

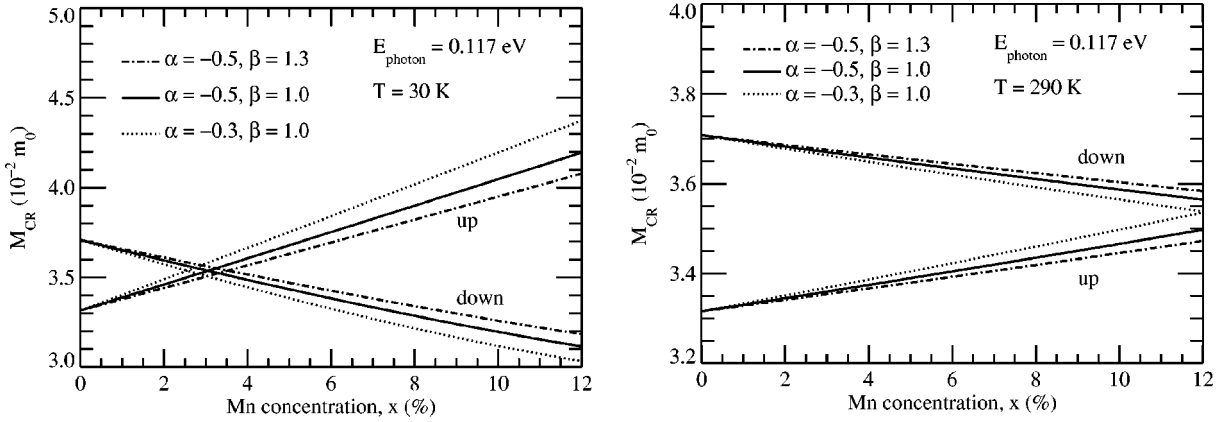


FIG. 11. Calculated electron cyclotron masses for the lowest-lying spin-up and spin-down Landau transitions in  $n$ -type  $\text{In}_{1-x}\text{Mn}_x\text{As}$  at  $\hbar\omega = 0.117$  eV as a function of Manganese concentration for (a)  $T = 30$  K and (b)  $T = 290$  K. Electron cyclotron masses are shown for three sets of  $\alpha$  and  $\beta$  values.

cyclotron absorption peaks observed at low electron density in Fig. 10(a) split into doublets in Fig. 10(b). At room temperature, the two lowest Landau levels are thermally populated and both spin-up and spin-down transitions appear in the cyclotron absorption spectra. The shift in the cyclotron absorption features with increasing Mn concentration is also different at room temperature. As  $x$  increases, we find that the cyclotron absorption features in Fig. 10(b) shift to higher fields. As we increase the temperature the magnitude of the average Mn spin  $\langle S_z \rangle$  described by the Brillouin function in Eq. (24) decreases. Since the exchange Hamiltonian  $H_{Mn}$  in Eq. (22) is proportional to  $x \langle S_z \rangle$ , the spin splittings reverse sign at higher Mn concentrations.

#### D. Electron cyclotron mass

The electron cyclotron mass  $M_{CR}$  for a given cyclotron absorption transition is related to the resonance field  $B^*$  (cyclotron energy  $\mu_B B^*$ ) and photon energy  $\hbar\omega$  by the definition

$$\frac{M_{CR}}{m_0} \equiv \frac{2\mu_B B^*}{\hbar\omega}. \quad (55)$$

In Fig. 11, the calculated cyclotron masses for the lowest spin-down [(b) set] transitions and spin-up [(a) set] transitions are plotted as a function of Mn concentration  $x$  at a photon energy of  $\hbar\omega = 0.117$  eV. Cyclotron masses are computed for several sets of  $\alpha$  and  $\beta$  values. The cyclotron masses in Fig. 11(a) and 11(b) correspond to the computed cyclotron absorption spectra shown in Figs. 10(a) and 10(b), respectively. In our model, the electron cyclotron masses shown depend on the Landau subband energies and photon energies and are independent of electron concentration (though, clearly, the population of a given state will depend upon the concentration).

In the Kane model discussed earlier, the cyclotron energy in  $\text{In}_{1-x}\text{Mn}_x\text{As}$  depends linearly on the Mn concentration  $x$ . In addition, the cyclotron mass, which is inversely proportional to the cyclotron resonance energy, increases for conduction electrons from the (a) subsystem and decreases for

conduction electrons in the (b) subsystem. These predictions of the simple Kane model are both confirmed as can be seen in Fig. 11.

The sensitivity of the cyclotron masses to  $\alpha$  and  $\beta$  seen in Fig. 11 can be understood if we study the dependence of the cyclotron energy on the exchange constants  $\alpha$  and  $\beta$  in the simple Kane model previously discussed. Because  $\text{InMnAs}$  is a narrow -gap semiconductor, it is not surprising that the conduction-band cyclotron energy should depend not only on the conduction-band exchange constant  $\alpha$  but also on the valence-band exchange constant  $\beta$ . This just reflects conduction-valence-band mixing in the magnetic field. Our Kane model calculations show, however, that only their difference is important and that only one independent constant ( $\alpha - \beta$ ) is needed to describe conduction-band cyclotron resonance with high accuracy. It is seen from Eqs. (37)–(40) that in the high-field limit the exchange interaction correction to the cyclotron energy is proportional to ( $\alpha - \beta$ ) while in the low-field limit the term proportional to ( $\alpha - \beta$ ) is one order of magnitude larger than the term proportional to  $\beta$ . Most of the important corrections to the cyclotron energy come from the heavy-hole admixture to conduction-band states. The difference ( $\alpha - \beta$ ) reflects the change in the band gap due to the exchange interaction and affects the degree of this mixing. This suggests that the dependence on ( $\alpha - \beta$ ) can be interpreted as just a renormalization of the band gap in a magnetic field.

Note that while Fig. 11 shows that the cyclotron peak positions are very sensitive to ( $\alpha - \beta$ ) [the figure shows how a 20% change in ( $\alpha - \beta$ ) can affect these positions], one can only measure the difference  $\alpha - \beta$  from these measurements and not  $\alpha$  and  $\beta$  independently. In addition, to determine ( $\alpha - \beta$ ) the other parameters (such as  $\gamma_1$ ,  $\gamma_2$ ,  $\gamma_3$ , etc.) must be accurately known.

#### E. Comparison with experiment

In this section, we compare the results of our theoretical calculations with our experimental results.

We first compute the near-band-gap absorption spectra for  $x = 0$  and 0.12. This is important since in our theoretical cal-

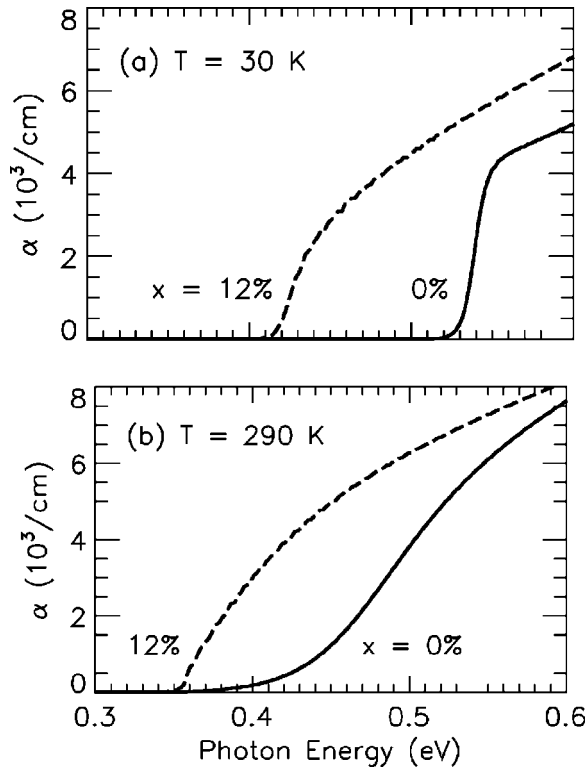


FIG. 12. Theoretical absorption coefficient for linear polarization as a function of photon energy at 30 K (a) and 290 K (b) at  $B=0$  for Mn concentrations  $x=0\%$  (solid lines) and  $x=12\%$  (dashed lines). Shifts in the band gaps are entirely due to carrier filling effects. These figures should be compared with the experimental data shown in Fig. 2.

culations, we have only included the effect of  $sp-d$  interaction of the Mn ions with the electrons and holes. An additional, nonmagnetic effect of the Mn ions could be to change the band gap with doping  $x$  similar to the band gap shift of  $\text{Al}_x\text{Ga}_{1-x}\text{As}$  with increasing Al content. Figures 12(a) and 12(b) show calculated near-band-gap absorption spectra for the  $x=0$  and 0.12 samples at (a) 30 K and (b) 290 K without taking into account a change in band gap with Mn doping. The theory successfully reproduces the experimental results shown in Fig. 2. The blueshift of the band gap in the  $x=0$  sample is entirely due to band filling effects, i.e., the Burstein-Moss shift. The  $x=0$  sample has a relatively high electron density. As Mn doping is increased, the electron density decreases since the Mn ion acts as an acceptor. The theory curves in the figure also show the sharpening of the band edge at low temperatures, consistent with the experiment. The fact that our theory curves are able to reproduce the  $x$  dependent absorption spectra without changing the band gap indicates that any  $x$  dependence to the band gap is small and we therefore neglect it.

Figures 13(a) and 13(b) show the calculated CR absorption coefficient for electron-active circularly polarized 10.6  $\mu\text{m}$  light in the Faraday configuration as a function of magnetic field at 30 K and 290 K, respectively. Densities for each sample are given in Table I. In the calculation, the curves were broadened based on the mobilities of the samples. The broadening used for  $T=30$  K was 4 meV for 0%, 40 meV for

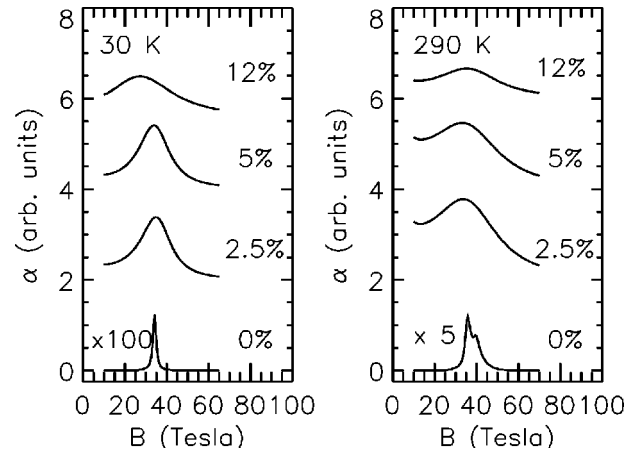


FIG. 13. Calculated CR absorption as a function of magnetic field at 30 K (a) and 290 K (b). The curves were calculated based on the Pidgeon-Brown model and the golden rule for absorption. The curves were broadened based on the mobilities reported in Table I.

2.5%, 40 meV for 5%, and 80 meV for 12%. For  $T=290$  K, the broadening used was 4 meV for 0%, 80 meV for 2.5%, 80 meV for 5%, and 80 meV for 12%.

At  $T=30$  K, we see a shift in the CR peak as a function of doping in agreement with Fig. 1(a). For  $T=290$  K, we see the presence of two peaks in the pure InAs sample. The second peak originates from the thermal population of the lowest spin-down Landau level. The peak does not shift as much with doping as it did at low temperature. This results from the temperature dependence of the average Mn spin. We believe that the Brillouin function used for calculating the average Mn spin becomes inadequate at large  $x$  and/or high temperature due to its neglect of Mn-Mn interactions such as pairing and clustering.

## V. SUMMARY AND CONCLUSIONS

We presented a theory for the electronic and magneto-optical properties in  $n$ -type narrow-gap  $\text{In}_{1-x}\text{Mn}_x\text{As}$  magnetic semiconductor alloys in an ultrahigh external magnetic field,  $B$ , oriented along [001]. We find several key results: (i) There is a shift in the cyclotron resonance with Mn doping which is not predicted in simple models. To lowest order, this shift depends upon  $(\alpha - \beta)$  and can be thought of as a renormalization of the energy gap in a magnetic field. The value of the energy gap influences the amount of conduction-valence-band mixing. (ii) Even with no Mn doping, there is spin splitting in the cyclotron resonance which results from the nonparabolicity of the conduction band in the narrow-gap material. (iii) The relative heights of the spin-split cyclotron absorption peaks can allow one to extract information about carrier density. (iv) At high temperatures and high ( $>10\%$ ) Mn concentrations, the calculated shift of the cyclotron resonance is not as large as the experimentally observed shift. This probably results from the inadequacy of the Brillouin function used for calculating the average Mn spin at large  $x$  and/or high temperature due to its neglect of Mn-Mn interactions such as pairing and clustering.

In modeling the cyclotron resonance experiments we used

an eight-band Pidgeon-Brown model generalized to include the wave vector dependence of the electronic states along  $k_z$  as well as the  $s$ - $d$  and  $p$ - $d$  exchange interactions with the localized Mn  $d$  electrons. Calculated conduction-band Landau levels exhibit effective masses and  $g$  factors that are strongly dependent on temperature, magnetic field, Mn concentration  $x$ , and  $k_z$ . At low temperatures and high  $x$ , the sign of the  $g$  factor is positive and its magnitude exceeds 100. CR spectra are computed using Fermi's golden rule and compared with ultrahigh-magnetic-field ( $> 50$  T) CR experiments, which show that the electron CR peak shifts sensitively with  $x$ . Detailed comparison between theory and experiment allowed us to extract the  $s$ - $d$  and  $p$ - $d$  exchange parameters  $\alpha$  and  $\beta$ . We showed that not only  $\alpha$  but also  $\beta$  affects the electron mass because of the strong interband coupling in this narrow-gap semiconductor. In addition, we derived analytical expressions for effective masses and  $g$  factors using the Kane model, which indicates that  $(\alpha - \beta)$  is the crucial parameter that determines the exchange interaction correction to the cyclotron masses. These findings should be useful for designing novel devices based on ferromagnetic semiconductors.

## ACKNOWLEDGMENTS

This work was supported by DARPA through Grant No. MDA972-00-1-0034, the National Science Foundation through Grant No. DMR 9817828, the NEDO International Joint Research Program and NSF Grant INT-0221704.

## APPENDIX A: LANDAU HAMILTONIAN

In this appendix, we write down the Landau contribution to the Hamiltonian in the matrix eigenvalue problem (28) for an arbitrary Landau quantum number  $n$ . The Landau Hamiltonian matrix can be obtained by taking the operator form of the Landau Hamiltonian in Eq. (7) and operating on the envelope function wave function (27), making use of the properties of the creation and destruction operators  $a^\dagger$  and  $a$ . The resulting matrix is

$$H'_L = \frac{\hbar^2}{m_0} \begin{bmatrix} L'_a & L'_c \\ L'_c^\dagger & L'_b \end{bmatrix}, \quad (\text{A1})$$

where the submatrices are given by

$$L'_a = \begin{bmatrix} E' + \frac{k^2}{2} + \gamma_4'' \left( n - \frac{1}{2} \right) & iV' \sqrt{n-1} & iV' \sqrt{\frac{1}{3}n} & V' \sqrt{\frac{2}{3}n} \\ -iV' \sqrt{n-1} & \left( \gamma_2 - \frac{\gamma_1}{2} \right) k^2 - \gamma_{12}(2n-3) & -\gamma_{23} \sqrt{3n(n-1)} & i\gamma_{23} \sqrt{6n(n-1)} \\ -iV' \sqrt{\frac{1}{3}n} & -\gamma_{23} \sqrt{3n(n-1)} & -\left( \gamma_2 + \frac{\gamma_1}{2} \right) k^2 - \bar{\gamma}_{12}(2n+1) & i\sqrt{2} \left[ -\gamma_2 k^2 + \gamma_2'' \left( n + \frac{1}{2} \right) \right] \\ V' \sqrt{\frac{2}{3}n} & -i\gamma_{23} \sqrt{6n(n-1)} & -i\sqrt{2} \left[ -\gamma_2 k^2 + \gamma_2'' \left( n + \frac{1}{2} \right) \right] & -\Delta' - \gamma_1 \frac{k^2}{2} - \gamma_1'' \left( n + \frac{1}{2} \right) \end{bmatrix}, \quad (\text{A2})$$

$$L'_b = \begin{bmatrix} E' + \frac{k^2}{2} + \gamma_4'' \left( n + \frac{1}{2} \right) & -V' \sqrt{n+1} & -V' \sqrt{\frac{1}{3}n} & iV' \sqrt{\frac{2}{3}n} \\ -V' \sqrt{n+1} & \left( \gamma_2 - \frac{\gamma_1}{2} \right) k^2 - \gamma_{12}(2n+3) & -\gamma_{23} \sqrt{3n(n+1)} & i\gamma_{23} \sqrt{6n(n+1)} \\ -V' \sqrt{\frac{1}{3}n} & -\gamma_{23} \sqrt{3n(n+1)} & -\left( \gamma_2 + \frac{\gamma_1}{2} \right) k^2 - \bar{\gamma}_{12}(2n-1) & i\sqrt{2} \left[ -\gamma_2 k^2 + \gamma_2'' \left( n - \frac{1}{2} \right) \right] \\ -iV' \sqrt{\frac{2}{3}n} & -i\gamma_{23} \sqrt{6n(n+1)} & -i\sqrt{2} \left[ -\gamma_2 k^2 + \gamma_2'' \left( n - \frac{1}{2} \right) \right] & -\Delta' - \gamma_1 \frac{k^2}{2} - \gamma_1'' \left( n - \frac{1}{2} \right) \end{bmatrix}, \quad (\text{A3})$$

$$L'_c = k \begin{bmatrix} 0 & 0 & V \sqrt{\frac{2}{3}} & iV \sqrt{\frac{1}{3}} \\ 0 & 0 & i\gamma_3' \sqrt{6(n-1)} & -\gamma_3' \sqrt{n-1} \\ -iV \sqrt{\frac{2}{3}} & -i\gamma_3' \sqrt{6(n+1)} & 0 & -3\gamma_3' \sqrt{n} \\ -V \sqrt{\frac{1}{3}} & \gamma_3' \sqrt{3(n+1)} & -3\gamma_3' \sqrt{n} & 0 \end{bmatrix}, \quad (\text{A4})$$

where  $k=k_z$  is the wave vector along the magnetic field direction, and  $n$  is the Landau quantum number for the manifold of states. The submatrix  $L_c^{\dagger}$  is obtained by taking the Hermitian adjoint of  $L_c'$ . In Eqs. (A2), (A3), and (A4) we make the following definitions:

$$E' = \frac{m_0}{\hbar^2} E_g, \quad (\text{A5})$$

$$\Delta' = \frac{m_0}{\hbar^2} \Delta, \quad (\text{A6})$$

$$V' = \frac{m_0}{\hbar^2} \frac{V}{\lambda}, \quad (\text{A7})$$

$$\gamma_i' = \frac{\gamma_i}{\lambda} \quad (i=1, \dots, 4), \quad (\text{A8})$$

$$\gamma_i'' = \frac{\gamma_i}{\lambda^2} \quad (i=1, \dots, 4), \quad (\text{A9})$$

$$\gamma_{ij} = \frac{1}{\lambda^2} \frac{\gamma_i + \gamma_j}{2} \quad (i, j=1, \dots, 4), \quad (\text{A10})$$

$$\bar{\gamma}_{ij} = \frac{1}{\lambda^2} \frac{\gamma_i - \gamma_j}{2} \quad (i, j=1, \dots, 4). \quad (\text{A11})$$

Here  $E_g$  and  $\Delta$  are the band gap and spin-orbit splitting energies,  $\lambda$  is the magnetic length defined in Eq. (6),  $V$  is the Kane momentum matrix element defined in Eq. (11), and the  $\gamma_i$ 's are the effective mass parameters defined in Eq. (12). The total Hamiltonian  $H_n$  to be diagonalized in the eigenvalue equation (28) is the sum of the Landau Hamiltonian matrix (A1) and the Zeeman and exchange Hamiltonians (18) and (22).

We note from Eq. (A4) that the submatrix  $L_c'$  is proportional to  $k$  and so vanishes at  $k=0$ . In this limit,  $H_n$  is block diagonal with respect to the upper and lower Bloch basis sets defined in Eqs. (1) and (2).

## APPENDIX B: OPTICAL MATRIX ELEMENTS

In this appendix we write down the momentum matrix elements used in the computation of optical matrix elements in Eq. (50). For the Bloch basis states defined in Eqs (1) and (2), the matrix elements for the momentum operators  $p_x$ ,  $p_y$ , and  $p_z$  are given by

$$P_x = \begin{bmatrix} 0 & iV\sqrt{\frac{1}{2}} & iV\sqrt{\frac{1}{6}} & V\sqrt{\frac{1}{3}} & 0 & 0 & 0 & 0 \\ -iV\sqrt{\frac{1}{2}} & 0 & 0 & 0 & 0 & 0 & 0 & 0 \\ -iV\sqrt{\frac{1}{6}} & 0 & 0 & 0 & 0 & 0 & 0 & 0 \\ V\sqrt{\frac{1}{3}} & 0 & 0 & 0 & 0 & 0 & 0 & 0 \\ 0 & 0 & 0 & 0 & 0 & -V\sqrt{\frac{1}{2}} & -V\sqrt{\frac{1}{6}} & iV\sqrt{\frac{1}{3}} \\ 0 & 0 & 0 & 0 & -V\sqrt{\frac{1}{2}} & 0 & 0 & 0 \\ 0 & 0 & 0 & 0 & -V\sqrt{\frac{1}{6}} & 0 & 0 & 0 \\ 0 & 0 & 0 & 0 & -iV\sqrt{\frac{1}{3}} & 0 & 0 & 0 \end{bmatrix}, \quad (\text{B1})$$

$$P_y = \begin{bmatrix} 0 & -V\sqrt{\frac{1}{2}} & V\sqrt{\frac{1}{6}} & -iV\sqrt{\frac{1}{3}} & 0 & 0 & 0 & 0 \\ -V\sqrt{\frac{1}{2}} & 0 & 0 & 0 & 0 & 0 & 0 & 0 \\ V\sqrt{\frac{1}{6}} & 0 & 0 & 0 & 0 & 0 & 0 & 0 \\ iV\sqrt{\frac{1}{3}} & 0 & 0 & 0 & 0 & 0 & 0 & 0 \\ 0 & 0 & 0 & 0 & 0 & iV\sqrt{\frac{1}{2}} & -iV\sqrt{\frac{1}{6}} & -V\sqrt{\frac{1}{3}} \\ 0 & 0 & 0 & 0 & -iV\sqrt{\frac{1}{2}} & 0 & 0 & 0 \\ 0 & 0 & 0 & 0 & iV\sqrt{\frac{1}{6}} & 0 & 0 & 0 \\ 0 & 0 & 0 & 0 & -V\sqrt{\frac{1}{3}} & 0 & 0 & 0 \end{bmatrix}, \quad (\text{B2})$$

$$P_z = \begin{bmatrix} 0 & 0 & 0 & 0 & 0 & 0 & V\sqrt{\frac{2}{3}} & iV\sqrt{\frac{1}{3}} \\ 0 & 0 & 0 & 0 & 0 & 0 & 0 & 0 \\ 0 & 0 & 0 & 0 & -iV\sqrt{\frac{2}{3}} & 0 & 0 & 0 \\ 0 & 0 & 0 & 0 & -V\sqrt{\frac{1}{3}} & 0 & 0 & 0 \\ 0 & 0 & iV\sqrt{\frac{2}{3}} & -V\sqrt{\frac{1}{3}} & 0 & 0 & 0 & 0 \\ 0 & 0 & 0 & 0 & 0 & 0 & 0 & 0 \\ V\sqrt{\frac{2}{3}} & 0 & 0 & 0 & 0 & 0 & 0 & 0 \\ -iV\sqrt{\frac{1}{3}} & 0 & 0 & 0 & 0 & 0 & 0 & 0 \end{bmatrix}, \quad (\text{B3})$$

where  $V$  is the Kane matrix element defined in Eq. (11).

\*Present address: Physics Department, University of Utah, Salt Lake City, Utah 84112, USA.

†Present address: Department of Physics, Faculty of Science, Okayama University, Okayama, Japan.

<sup>1</sup>H. MuneKata, H. Ohno, S. von Molnár, A. Segmüller, L. L. Chang, and L. Esaki, *Phys. Rev. Lett.* **63**, 1849 (1989).

<sup>2</sup>H. Ohno, A. Shen, F. Matsukara, A. Oiwa, A. Endo, S. Katsumoto, and Y. Iye, *Appl. Phys. Lett.* **69**, 363 (1996).

<sup>3</sup>S. Koshihara, A. Oiwa, M. Hirasawa, S. Katsumoto, Y. Iye, C. Urano, H. Takagi, and H. MuneKata, *Phys. Rev. Lett.* **78**, 4617 (1997).

<sup>4</sup>H. Ohno, D. Chiba, F. Matsukara, T. Omiya, E. Abe, T. Dietl, Y. Ohno, and K. Ohtani, *Nature (London)* **408**, 944 (2000).

<sup>5</sup>H. Ohno, H. MuneKata, T. Penney, S. von Molnár, and L. L. Chang, *Phys. Rev. Lett.* **68**, 2664 (1992).

<sup>6</sup>H. MuneKata, A. Zaslavski, P. Fumagalli, and R. J. Gambino, *Appl. Phys. Lett.* **63**, 2929 (1993).

<sup>7</sup>J. K. Furdyna, *J. Appl. Phys.* **64**, R29 (1988).

<sup>8</sup>Y. H. Matsuda, T. Ikaida, N. Miura, S. Kuroda, F. Takano, and K. Takita, *Phys. Rev. B* **65**, 115202 (2002).

<sup>9</sup>M. A. Zudov, J. Kono, Y. H. Matsuda, T. Ikaida, N. Miura, H. MuneKata, G. D. Sanders, Y. Sun, and C. J. Stanton, *Phys. Rev. B* **66**, 161307(R) (2002).

<sup>10</sup>K. Nakao, F. Herlach, T. Goto, S. Takeyama, T. Sakakibara, and N. Miura, *J. Phys. E* **18**, 1018 (1985).

<sup>11</sup>C. K. Pidgeon and R. N. Brown, *Phys. Rev.* **146**, 575 (1966).

- <sup>12</sup>J. Kossut, *Semicond. Semimetals* **25**, 183 (1988).
- <sup>13</sup>A. L. Efros and M. Rosen, *Phys. Rev. B* **58**, 7120 (1988).
- <sup>14</sup>I. Vurgaftman, J. R. Meyer, and L. R. Ram-Mohan, *J. Appl. Phys.* **89**, 5815 (2001).
- <sup>15</sup>J. M. Luttinger, *Phys. Rev.* **102**, 1030 (1956).
- <sup>16</sup>G. Dresselhaus, A. F. Kip, and C. Kittel, *Phys. Rev.* **98**, 368 (1955).
- <sup>17</sup>G. Dresselhaus, *Phys. Rev.* **100**, 580 (1955).
- <sup>18</sup>H. Munekata, H. Ohno, S. von Molnár, A. Harwitt, A. Segmüller, and L. L. Chang, *J. Vac. Sci. Technol. B* **8**, 176 (1990).
- <sup>19</sup>H. Ohno, H. Munekata, S. von Molnár, and L. L. Chang, *J. Appl. Phys.* **69**, 6103 (1991).
- <sup>20</sup>S. von Molnár, H. Munekata, H. Ohno, and L. L. Chang, *J. Magn. Mater.* **93**, 356 (1991).
- <sup>21</sup>E. O. Kane, *J. Phys. Chem. Solids* **1**, 249 (1957).
- <sup>22</sup>J. G. Mavroides, in *Optical Properties of Solids*, edited by F. Abelès (North-Holland, Amsterdam, 1972), pp. 351–528.
- <sup>23</sup>W. Zawadzki, in *Landau Level Spectroscopy*, edited by G. Landwehr and E. I. Rashba (North-Holland, Amsterdam, 1991), Vol. 1, pp. 483–512.
- <sup>24</sup>M. A. Kinch and D. D. Buss, *J. Phys. Chem. Solids* **32**, 461 (1971).
- <sup>25</sup>B. D. McCombe and R. J. Wagner, in *Proceedings of the 11th International Conference on the Physics of Semiconductors*, edited by M. Miasek (PWN-Polish Science, Warsaw, 1972), p. 321.
- <sup>26</sup>B. D. McCombe and R. J. Wagner, in *Advances in Electronics and Electron Physics*, edited by L. Marton (Academic Press, New York, 1975), pp. 1–78.
- <sup>27</sup>L. M. Roth, B. Lax, and S. Swerdling, *Phys. Rev.* **114**, 90 (1959).
- <sup>28</sup>F. Bassani and G. P. Parravicini, *Electronic States and Optical Transitions in Solids* (Pergamon, New York, 1975).
- <sup>29</sup>Y. P. Varshni, *Physica (Amsterdam)* **34**, 149 (1967).
- <sup>30</sup>E. D. Palik and R. F. Willis, *Phys. Rev.* **123**, 131 (1961).
- <sup>31</sup>J. I. Pankove, *Optical Processes in Semiconductors* (Dover, New York, 1971).
- <sup>32</sup>C. Rigaux, *Semicond. Semimetals* **25**, 229 (1988).